

TRACTABLE OPTIMAL EXPERIMENTAL DESIGN USING TRANSPORT MAPS

KARINA KOVAL, ROLAND HERZOG, AND ROBERT SCHEICHL

ABSTRACT. We present a flexible method for computing Bayesian optimal experimental designs (BOEDs) for inverse problems with intractable posteriors. The approach is applicable to a wide range of BOED problems and can accommodate various optimality criteria, prior distributions and noise models. The key to our approach is the construction of a transport-map-based surrogate to the joint probability law of the design, observational and inference random variables. This order-preserving transport map is constructed using tensor trains and can be used to efficiently sample from (and evaluate approximate densities of) conditional distributions that are required in the evaluation of many commonly-used optimality criteria. The algorithm is also extended to sequential data acquisition problems, where experiments can be performed in sequence to update the state of knowledge about the unknown parameters. The sequential BOED problem is made computationally feasible by preconditioning the approximation of the joint density at the current stage using transport maps constructed at previous stages. The flexibility of our approach in finding optimal designs is illustrated with some numerical examples inspired by disease modeling and the reconstruction of subsurface structures in aquifers.

1. INTRODUCTION

The Bayesian approach to parameter estimation is widespread throughout the sciences and engineering. In the Bayesian framework, a-priori knowledge (encoded in a prior measure) of some unknown/unobservable parameters is updated using experimental data and a mathematical model. Hence, the solution to the Bayesian inverse problem is a posterior probability law describing the updated state of knowledge conditioned on the observed data. The quality of the solution is highly dependent on the observed experimental data — a poorly-chosen experimental setup can lead to uninformed posteriors not straying far from the prior, whereas well-chosen experimental designs can lead to well-informed posteriors characterized by high degrees of certainty.

In many Bayesian inverse problems stemming from real-world phenomena, there are limitations on the number of experiments that can be performed or the amount of data that can be acquired. These limitations could originate from physical or monetary constraints. For example, tsunami warning systems rely on pressure sensors tethered to the ocean floor near trenches, and groundwater monitoring systems require drilling wells deep into the ground — both scenarios are characterized by expensive means of data acquisition. In such settings, it is crucial to allocate the limited resources well, choosing experimental conditions that maximize the “quality” of the measured data.

Optimal experimental design (OED) provides a rigorous mathematical framework for addressing the question of how to design experimental conditions for optimal parameter inference. Standard OED references in the point estimation setting include [49, 53, 50, 8], and the techniques found therein have gained much traction within the last few decades in the Bayesian inverse problems community. In OED, experimental designs are chosen to optimize some utility function that assesses the amount of information that could be gleaned from performing any feasible experiment. The utility functions are user-specified and problem-dependent, though there is a plethora of commonly used criteria. For any design, these commonly used criteria (e.g., A-, D-, E-optimality [1]) evaluate the statistical quality of

2010 *Mathematics Subject Classification.* 62K05, 62F15, 65K10, 65L09, 65N21, 15A69.

Key words and phrases. optimal experimental design, Bayesian inverse problems, uncertainty quantification, transportation of measures, low-rank tensor decomposition, tensor trains.

This work has been partially funded by Carl Zeiss-Stiftung through the project “Model-Based AI: Physical Models and Deep Learning for Imaging and Cancer Treatment”. RS and KK would like to thank the Isaac Newton Institute for Mathematical Sciences for support and hospitality during the programme on *Future Data-Driven Engineering* when part of the work on this paper was undertaken, supported by EPSRC grant number EP/R014604/1.

the resulting posterior distribution. The overarching goal is to choose designs or experimental conditions that minimize the level of uncertainty, or maximize information, in the posterior.

Solving the OED optimization problem is challenging for Bayesian inverse problems governed by models that involve systems of ordinary differential equations (ODEs) or even partial differential equations (PDEs). Since the Bayesian inverse problem is merely a sub-problem of OED, all the numerical challenges present in Bayesian inference due to, e.g., the large number of inference parameters or the high cost in evaluating the PDE/ODE models, are inherited. Many efficient and scalable algorithms for solving these challenging high-dimensional (or infinite-dimensional) OED problems have been developed in recent years [37, 4, 36, 2, 5, 45, 28, 1, 6, 27, 3, 10, 11, 55]. A large portion of these techniques (see, e.g., [33, 4, 7, 9, 45, 38, 6, 10]) are formulated for *linear* Bayesian inverse problems with additive Gaussian noise models and Gaussian priors. For such problems, the parameter enters linearly into the parameter-to-observable (PTO) map and the posteriors are Gaussian, hence simple to characterize.

In this article, we focus on the design of experimental conditions for Bayesian inverse problems governed by *nonlinear* PTO maps resulting in Bayesian inverse problems characterized by non-Gaussian posteriors. The nonlinear parameter-to-observable map introduces some unique challenges that are not present in the linear OED setting, even under the assumption of an additive Gaussian noise model — the most notable of which are lack of a closed-form expression for the utility function, and the dependence of the optimality criterion on the observed data. The latter issue is often circumvented by finding designs that work well on average for all realizations of the data, i.e., by optimizing the expected value of the chosen utility function. However, even after this simplification, the challenge of approximating the resulting objective function remains. A few common approaches to alleviate this involve: linearization techniques (e.g., using a Laplace approximation as in [42, 5]) or purely sample-based nested Monte Carlo techniques, made computationally feasible via surrogates of the parameter-to-observable map [37, 55].

Our approach. In this paper, we follow the latter set of techniques, i.e., to design computationally tractable sample-based approximations to the expected utility function. This is achieved by building a transport map that pushes forward a tractable reference density (e.g., multivariate Gaussian) to the intractable *joint* density for the design, observation and inference random variables. This transport map can be used to obtain independent and identically distributed (i.i.d.) samples for Monte Carlo approximation to the expected utility for any feasible design and various choices of the utility function.

Transport maps have been used for modeling and exploring posterior distributions in Bayesian inverse problems (see, e.g., [44, 48, 14, 16]), and have also made an appearance in the OED literature (see, e.g., [35, 12]). In [12], sample-based transport maps are used to approximate the information contained in various summary statistics of image data, with the ultimate goal of reducing data volume. In contrast, our focus is choosing experimental conditions that maximize information content of sparse data. Since the data distribution in our applications depends on the design, we learn the joint density for the data, inference parameter, and design random variables. This enables approximation of the expected utility function for various designs using a single transport map. In [35], a transport map to the joint density on the designs, observations and inference parameters is also constructed, but our approach differs in the following key ways: (i) we employ a functional tensor train (FTT)-based transport map following [21] and thus take a function approximation viewpoint rather than a sample-based density approximation approach; (ii) we target a wide class of Bayesian experimental design problems and optimality criteria, whereas the aforementioned work deals primarily with finding sequential optimal designs (SOEDs) maximizing expected information gain.

Contributions. The main contributions of the work presented here are as follows: (i) We formulate a computationally tractable transport map approach for approximating expected utility functions appearing in Bayesian OED problems. The approach presented is applicable to a wide range of optimality criteria, design types, and prior models, and is thus highly flexible. (ii) We extend the base methodology for finding sequentially optimal designs in a greedy fashion. To make the sequential OED procedure computationally feasible, we propose recycling previously learned information into suitably chosen preconditioners to speed up subsequent computations. (iii) We present a numerical study that illustrates the effectiveness and flexibility of the proposed approach for two types of design problems.

Limitations and outlook. Of course, the approach is not without limitations: (i) While the approach works well in practice for problems with a *moderate* number of inference parameters, the presented algorithms are typically infeasible for very high- or infinite-dimensional problems. This can be circumvented with a-priori dimensionality reduction using, e.g., an extension of the reparametrization techniques presented in [21, Section 3]. (ii) Likewise, the approach works well for finding optimal designs for a small to moderate number of experiments, i.e., in the small data regime, which is the primary focus in this article. (iii) It is clear from the design comparisons presented in Section 6 that the approach seems to work well in practice, however, a theoretical study of the approximation error and rank bounds for the FTT-based surrogates will be crucial to garner a better understanding of the suitability and limitations of our approach. First steps to obtain such theoretical guarantees for Gaussian densities can be found in [51].

Outline. In Section 2 we outline relevant prerequisite material on the Bayesian approach to inverse problems and Bayesian optimal experimental design. In Section 3 we use the Knothe-Rosenblatt rearrangement for defining transport-map-based approximations to OED objective functions. A tractable tensor train construction of the transport maps (building on [21]) is presented in Section 4. Section 5 extends our method for guiding data acquisition in a sequential fashion, i.e., for adaptive OED. In Section 6, we illustrate our method with two numerical examples.

2. BACKGROUND

In Section 2.1, we present some relevant preliminary material on Bayesian inverse problems characterized by non-Gaussian posteriors. We outline the basics of optimal experimental design for such problems as well as the related computational challenges in Section 2.2.

2.1. Bayesian inverse problems. We consider the inverse problem of inferring an unknown/unobservable vector of parameters $\mathbf{m} \in \mathcal{M}$ from observations of a quantity $\mathbf{d} \in \mathcal{D}$, related to $\mathbf{m} = [m_1, m_2, \dots, m_{n_m}]^T$ through the model:

$$(2.1) \quad \mathbf{d} = \mathcal{F}(\mathbf{m}) + \boldsymbol{\eta},$$

where $\mathcal{F}: \mathcal{M} \rightarrow \mathcal{D}$ denotes the parameter-to-observable (PTO) map and $\boldsymbol{\eta} \in \mathbb{R}^{n_d}$ refers to the measurement noise. The problem-dependent parameter space $\mathcal{M} \subseteq \mathbb{R}^{n_m}$ and observation space $\mathcal{D} \subseteq \mathbb{R}^{n_d}$ are assumed to be finite-dimensional. Additionally, we make the common assumption of an additive Gaussian noise model, though our method could be extended to incorporate other noise models. In many typical applications, $\mathcal{F} := \mathcal{O} \circ \mathcal{G}$ is defined as the composition of a parameter-to-state map $\mathcal{G}: \mathbb{R}^{n_m} \rightarrow \mathcal{U}$, where \mathcal{U} can denote a finite-dimensional or infinite-dimensional vector space, and an observation operator $\mathcal{O}: \mathcal{U} \rightarrow \mathbb{R}^{n_d}$. The observation operator maps the state $u \in \mathcal{U}$ to the observable quantity $\mathbf{d} = [d_1, d_2, \dots, d_{n_d}]^T$. For example, in the simplest case, \mathcal{O} can denote a (smoothed) point evaluation operator. Of particular interest in this work are inverse problems where the parameter-to-state operator is expensive to apply, e.g., the parameter-to-state or *forward map* could be defined implicitly through the solution of a PDE or a system of ODEs. In this case, the parameter vector \mathbf{m} typically parametrizes some functional input to the forward operator.

The Bayesian approach is a probabilistic approach to solving inverse problems. Given a prior probability measure on \mathbf{m} , denoted by $\mu_{\mathbf{m}}$ with corresponding Lebesgue density $\pi_{\mathbf{m}}$, and mean-zero additive Gaussian noise, $\boldsymbol{\eta} \sim \mathcal{N}(\mathbf{0}, \Gamma_{\boldsymbol{\eta}})$, the solution to the Bayesian inverse problem is a posterior probability law. In the finite-dimensional parameter inference setting, the posterior law has a corresponding posterior density that can be obtained using Bayes' law,

$$(2.2) \quad \pi_{\mathbf{m}|\mathbf{d}} = \frac{\pi_{\mathbf{d}|\mathbf{m}} \pi_{\mathbf{m}}}{\pi_{\mathbf{d}}}.$$

The conditional density $\pi_{\mathbf{d}|\mathbf{m}}$, the so-called likelihood, satisfies $\pi_{\mathbf{d}|\mathbf{m}}(\mathbf{d} | \mathbf{m}) \propto \exp(-\frac{1}{2} \|\mathcal{F}(\mathbf{m}) - \mathbf{d}\|_{\Gamma_{\boldsymbol{\eta}}^{-1}}^2)$ due to the assumption of additive Gaussian measurement noise. Throughout, for any symmetric positive-definite matrix $\mathbf{W} \in \mathbb{R}^{n \times n}$ we use $\|\cdot\|_{\mathbf{W}}$ to denote the \mathbf{W} -weighted norm, i.e., for any $\mathbf{x} \in \mathbb{R}^n$, $\|\mathbf{x}\|_{\mathbf{W}}^2 := \mathbf{x}^T \mathbf{W} \mathbf{x}$. The so-called evidence $\pi_{\mathbf{d}}$ is typically unknown.

We note that for Bayesian inverse problems where the parameter \mathbf{m} enters nonlinearly into \mathcal{F} , the posterior $\pi_{\mathbf{m}|\mathbf{d}}$ is typically non-Gaussian and often there is no closed-form expression for the density (even under the assumption of Gaussian prior and additive Gaussian noise). In such cases, one can only probe the posterior distribution, e.g., by computing various moments or statistics like the maximum a-posteriori estimator (commonly referred to as the MAP point) using sampling techniques such as Markov chain Monte Carlo (MCMC) [34]. A similar situation arises for linear PTO maps when the prior is non-Gaussian.

2.2. Optimal experimental design with non-Gaussian posteriors. The quality of the solution to the Bayesian inverse problem depends crucially on the quality and quantity of the measured data. Guiding data acquisition or choosing experimental conditions for “optimal” inference of the unknown parameters \mathbf{m} requires solving an optimal experimental design problem. The definition of “experimental design” is typically problem-specific. For example, in sensor placement problems, the design could correspond to the spatial coordinates at which the state u is observed. Alternatively, the design could enter the PTO map \mathcal{G} *intrusively* as a boundary/initial condition, making the state design-dependent.

In the following, we assume that the design can be expressed using the variable $\mathbf{e} \in \mathcal{E} \subset \mathbb{R}^{n_e}$ and enters into the model through the parameter-to-observable map ($\mathcal{F}: \mathcal{E} \times \mathcal{M} \rightarrow \mathcal{D}$) as well as the noise model ($\boldsymbol{\eta} \sim \mathcal{N}(\mathbf{0}, \mathbf{\Gamma}_{\boldsymbol{\eta}}(\mathbf{e}))$). This includes both intrusive and non-intrusive designs. The design dependence of the model and thus of the likelihood $\pi_{\mathbf{d}|\mathbf{e},\mathbf{m}}(\mathbf{d}|\mathbf{e},\mathbf{m}) \propto \exp(-\frac{1}{2}\|\mathcal{F}(\mathbf{e},\mathbf{m}) - \mathbf{d}\|_{\mathbf{\Gamma}_{\boldsymbol{\eta}}(\mathbf{e})}^2)$ leads to a design-dependent posterior distribution with density

$$(2.3) \quad \pi_{\mathbf{m}|\mathbf{e},\mathbf{d}} = \frac{\pi_{\mathbf{d}|\mathbf{e},\mathbf{m}} \pi_{\mathbf{m}}}{\pi_{\mathbf{d}|\mathbf{e}}},$$

where we employed the common assumption that prior and design are independent, i.e., $\pi_{\mathbf{m}|\mathbf{e}} \equiv \pi_{\mathbf{m}}$.

Similar to the definition of design, what defines an “optimal” design is also problem-specific. For Bayesian inverse problems with non-Gaussian posteriors, optimal designs are often chosen to optimize some expected utility function, i.e.,

$$(2.4) \quad \mathbf{e}^* \in \underset{\mathbf{e} \in \mathcal{E}}{\text{Arg max}} \mathbb{E}_{\pi_{\mathbf{d}|\mathbf{e}}} [\psi(\mathbf{e}, \mathbf{d})].$$

For any design $\mathbf{e} \in \mathcal{E}$ and corresponding measured data $\mathbf{d} \in \mathcal{D}$, the utility function $\psi(\mathbf{e}, \mathbf{d})$ evaluates the quality of the solution to the resulting Bayesian inverse problem. This risk-neutral formulation chooses designs that maximize the user-specified utility function on average for all possible realizations of the data. There are many options for the utility function leading to different optimal designs. For illustrative purposes we focus on two commonly used criteria in the Bayesian OED literature: A- and D-optimality.

The *A-optimality* criterion seeks designs that minimize the expected value of the average posterior variance in the inference parameters. This is equivalent to maximizing the expected value of the A-optimal utility function ψ_A , defined as

$$(2.5) \quad \psi_A(\mathbf{e}, \mathbf{d}) := -\text{trace}[\mathbf{C}_{\mathbf{m}|\mathbf{e},\mathbf{d}}(\mathbf{e}, \mathbf{d})].$$

Here $\mathbf{C}_{\mathbf{m}|\mathbf{e},\mathbf{d}}(\mathbf{e}, \mathbf{d}) = \mathbb{E}_{\pi_{\mathbf{m}|\mathbf{e},\mathbf{d}}} [(\mathbf{m} - \mathbf{m}_{\text{post}}^{\mathbf{e},\mathbf{d}})(\mathbf{m} - \mathbf{m}_{\text{post}}^{\mathbf{e},\mathbf{d}})^T]$ denotes the posterior covariance matrix with posterior mean $\mathbf{m}_{\text{post}}^{\mathbf{e},\mathbf{d}} := \mathbb{E}_{\pi_{\mathbf{m}|\mathbf{e},\mathbf{d}}}[\mathbf{m}]$.

On the other hand, the Bayesian *D-optimal* design maximizes the *expected information gain* (EIG) from prior to posterior (see, e.g., [40]). Thus the D-optimal utility function ψ_D is defined as the Kullback-Leibler (KL) divergence of the posterior from the prior,

$$(2.6) \quad \psi_D(\mathbf{e}, \mathbf{d}) := \mathcal{D}_{\text{KL}}(\pi_{\mathbf{m}|\mathbf{e},\mathbf{d}} \| \pi_{\mathbf{m}}) = \mathbb{E}_{\pi_{\mathbf{m}|\mathbf{e},\mathbf{d}}} \left[\log \left(\frac{\pi_{\mathbf{m}|\mathbf{e},\mathbf{d}}}{\pi_{\mathbf{m}}} \right) \right].$$

We emphasize that for non-Gaussian posteriors, there are typically no closed-form expressions for the utility functions ψ_A and ψ_D . Thus, it is a significant challenge to evaluate these criteria and their expected values, denoted respectively by Ψ_A and Ψ_D . To address the latter, we take a sample average

approximation (SAA) approach, which leads to the discretized A- and D-optimality criteria:

$$(2.7) \quad \Psi_A(\mathbf{e}) \approx -\frac{1}{N} \sum_{i=1}^N \text{trace}[\mathbf{C}_{\mathbf{m}|\mathbf{e}, \mathbf{d}^{(i)}}(\mathbf{e}, \mathbf{d}^{(i)})] =: \hat{\Psi}_A^N(\mathbf{e})$$

$$(2.8) \quad \Psi_D(\mathbf{e}) = \mathbb{E}_{\pi_{\mathbf{d}, \mathbf{m}|\mathbf{e}}} \left[\log \left(\frac{\pi_{\mathbf{m}|\mathbf{e}, \mathbf{d}}}{\pi_{\mathbf{m}}} \right) \right] \approx \frac{1}{N} \sum_{i=1}^N \log \left(\frac{\pi_{\mathbf{m}|\mathbf{e}, \mathbf{d}^{(i)}}(\mathbf{m}^{(i)})}{\pi_{\mathbf{m}}(\mathbf{m}^{(i)})} \right) =: \hat{\Psi}_D^N(\mathbf{e}).$$

The first equality in (2.8) is obtained via another application of Bayes' law.

However, the aforementioned challenge of evaluating the summands remains. Exact evaluation of each summand is generally infeasible, and some efficient approximation is needed. These approximations typically require access to the posterior distribution for many realizations of the data and design. Additionally, in defining both criteria, we have assumed the ability to sample from generally intractable distributions, i.e., $\mathbf{d}^{(i)} \sim \pi_{\mathbf{d}|\mathbf{e}}$ in (2.7) and $(\mathbf{d}^{(i)}, \mathbf{m}^{(i)}) \sim \pi_{\mathbf{d}, \mathbf{m}|\mathbf{e}}$ in (2.8) for any design choice $\mathbf{e} \in \mathcal{E}$. While efficient MCMC methods for obtaining these samples and thus exploring intractable distributions have been developed in recent years (see, e.g., [24, 22]), using these approaches to solve the OED problem would require generating a different set of samples for each design realization in an iterative optimization algorithm, which can get prohibitively expensive and leads to noisy evaluations of the utility function.

Instead, we employ a measure-transport approach that enables rapid sampling from the joint density $\pi_{\mathbf{d}, \mathbf{m}|\mathbf{e}}$, the marginal $\pi_{\mathbf{d}|\mathbf{e}}$, and posterior $\pi_{\mathbf{m}|\mathbf{d}, \mathbf{e}}$ for any fixed design. The idea, which builds on [21], is to construct a deterministic coupling between a product-form reference distribution $\nu_{\mathbf{e}, \mathbf{d}, \mathbf{m}}$ and the joint distribution for the design, observational and inference random variables $\mu_{\mathbf{e}, \mathbf{d}, \mathbf{m}}$. A particular choice of this coupling, or transport map, called the Knothe-Rosenblatt rearrangement, “exposes” conditional densities and is thus crucial for our approach.

3. OPTIMAL EXPERIMENTAL DESIGN USING TRANSPORT MAPS

In this section we present a flexible transport map approach to OED for a wide class of Bayesian inverse problems. A crucial tool for realizing our approach is the Knothe-Rosenblatt rearrangement, which we define in Section 3.1. In Section 3.2 and Section 3.3, we outline how the KR map can be used to approximate the OED objective function (2.4) with particular emphasis on A- and D-optimality. Error bounds are discussed in Section 3.4 with an emphasis on the D-optimal design.

3.1. Conditional sampling via Knothe-Rosenblatt transport. Given a target random variable $\mathbf{x} = [x_1, \dots, x_n]^T \in \mathbb{R}^n$ and a reference random variable $\mathbf{v} = [v_1, \dots, v_n]^T \in \mathbb{R}^n$ with probability laws $\mu_{\mathbf{x}}$ and $\nu_{\mathbf{v}}$, respectively, the *Knothe-Rosenblatt* (KR) rearrangement ([52, 54]) defines a triangular, order-preserving diffeomorphism $\mathcal{T}: \mathbb{R}^n \rightarrow \mathbb{R}^n$ that couples \mathbf{x} and \mathbf{v} . The general structure of \mathcal{T} is

$$(3.1) \quad \mathcal{T}(\mathbf{v}) = \begin{bmatrix} x_1 \\ x_2 \\ \vdots \\ x_n \end{bmatrix} = \begin{bmatrix} \mathcal{T}_{x_1}(v_1) \\ \mathcal{T}_{x_2|x_1}(\mathbf{v}_{1:2}) \\ \vdots \\ \mathcal{T}_{x_n|\mathbf{x}_{1:n-1}}(\mathbf{v}) \end{bmatrix},$$

where the notation $\mathbf{x}_{1:k} = [x_1, x_2, \dots, x_k]$ is used to denote the first k components of \mathbf{x} . Note that by *order-preserving*, we mean that each component $\mathcal{T}_{x_k|\mathbf{x}_{1:k-1}}: \mathbb{R}^k \rightarrow \mathbb{R}$ is strictly monotonically increasing in the last variable, v_k . Under this map, the *pushforward* of $\nu_{\mathbf{v}}$ is the law of the image $\mathcal{T}(\mathbf{v})$ and is denoted by $\mathcal{T}_\# \nu_{\mathbf{v}}$. The *pullback* of $\mu_{\mathbf{x}}$ is the law of $\mathcal{T}^{-1}(\mathbf{x})$ denoted by $\mathcal{T}^\# \mu_{\mathbf{x}}$. In other words, if $\mathbf{v} \sim \nu_{\mathbf{v}}$, then $\mathcal{T}(\mathbf{v}) \sim \mu_{\mathbf{x}}$. Thus, \mathcal{T} provides a means of transforming samples distributed according to the reference measure $\nu_{\mathbf{v}}$ to samples distributed according to the target measure $\mu_{\mathbf{x}}$.

We only consider measures that are absolutely continuous with respect to the Lebesgue measure. A unique KR rearrangement exists in such cases, and the pushforward and pullback operators define

transformations between the target density $\pi_{\mathbf{x}}$ (corresponding to $\mu_{\mathbf{x}}$) and the reference density $\rho_{\mathbf{v}}$ (corresponding to $\nu_{\mathbf{v}}$) via the change-of-variables formulae

$$(3.2) \quad \pi_{\mathbf{x}}(\mathbf{x}) = \mathcal{T}_{\#} \rho_{\mathbf{v}}(\mathbf{x}) = \rho_{\mathbf{v}}(\mathcal{T}^{-1}(\mathbf{x})) \det(D\mathcal{T}^{-1}(\mathbf{x})),$$

$$(3.3) \quad \rho_{\mathbf{v}}(\mathbf{v}) = \mathcal{T}^{\#} \pi_{\mathbf{x}}(\mathbf{v}) = \pi_{\mathbf{x}}(\mathcal{T}(\mathbf{v})) \det(D\mathcal{T}(\mathbf{v})),$$

where D denotes the Jacobian of the respective map. Note that as a consequence of these formulae,

$$(3.4) \quad \mathbb{E}_{\pi_{\mathbf{x}}}[g] = \mathbb{E}_{\rho_{\mathbf{v}}}[g \circ \mathcal{T}]$$

for any measurable function g on \mathbb{R}^n . Henceforth we assume $\rho_{\mathbf{v}}$ is a product-form reference density, i. e., it can be written as the product of its marginals, $\rho_{\mathbf{v}} = \prod_{i=1}^n \rho_{v_i}(v_i)$.

Not only does the KR rearrangement offer computational benefits due to its triangular structure, the map also “exposes” particular conditionals of the density $\pi_{\mathbf{x}}$. Let $\mathbf{x} = (\mathbf{y}, \mathbf{z})$ be a partition of the target random variable with $\mathbf{y} \in \mathbb{R}^{n_y}$, $\mathbf{z} \in \mathbb{R}^{n_z}$ and $n = n_y + n_z$. Then (3.1) can be written as

$$(3.5) \quad \mathcal{T}(\mathbf{v}) := \mathcal{T}(\mathbf{v}_y, \mathbf{v}_z) = \begin{bmatrix} \mathcal{T}_{\mathbf{y}}(\mathbf{v}_y) \\ \mathcal{T}_{\mathbf{z}|\mathbf{y}}(\mathbf{v}_y, \mathbf{v}_z) \end{bmatrix},$$

where $\mathbf{v}_y \in \mathbb{R}^{n_y}$, $\mathbf{v}_z \in \mathbb{R}^{n_z}$, $\mathcal{T}_{\mathbf{y}}: \mathbb{R}^{n_y} \rightarrow \mathbb{R}^{n_y}$ and $\mathcal{T}_{\mathbf{z}|\mathbf{y}}: \mathbb{R}^{n_y} \times \mathbb{R}^{n_z} \rightarrow \mathbb{R}^{n_z}$. For any fixed $\mathbf{y}^* \in \mathbb{R}^{n_y}$, the map $\mathcal{T}^{\mathbf{y}^*}: \mathbb{R}^{n_z} \rightarrow \mathbb{R}^{n_z}$ (defined as $\mathbf{v}_z \mapsto \mathcal{T}_{\mathbf{z}|\mathbf{y}}(\mathcal{T}_{\mathbf{y}}^{-1}(\mathbf{y}^*), \mathbf{v}_z)$) prescribes a coupling between the marginal reference density $\rho_{\mathbf{v}_z}$ and the conditional target density $\pi_{\mathbf{z}|\mathbf{y}=\mathbf{y}^*}$, i. e. $(\mathcal{T}^{\mathbf{y}^*})_{\#} \rho_{\mathbf{v}_z} = \pi_{\mathbf{z}|\mathbf{y}=\mathbf{y}^*}$ [43, Lemma 1].

This property makes the KR rearrangement particularly useful for conditional sampling, and we will exploit this feature for our OED approach. However, construction of the true map \mathcal{T} is in general not feasible and various approximation techniques have been developed. The most common technique is to define \mathcal{T} as the minimizer of some statistical divergence between the target density $\pi_{\mathbf{x}}$ and the pushforward of the reference $\mathcal{T}_{\#} \rho_{\mathbf{v}}$ over some parametrized class of triangular transport maps. These techniques use polynomials ([44, 14]) or kernel functions ([41, 23]) to approximate \mathcal{T} , as well as invertible neural networks and normalizing flows ([39, 13, 47]). In contrast, our approach uses the techniques outlined in [25, 20, 21] and constructs an explicit transport map to an approximation of the target density, but we delay those details to Section 4 and first discuss how the KR rearrangement could be used for approximating the OED objective function.

3.2. Knothe-Rosenblatt rearrangement for OED. At the core of our approach is the approximation of the joint density $\pi_{\mathbf{e}, \mathbf{d}, \mathbf{m}}$ for the design, observable and inference parameters by the pushforward of a product-form reference density $\rho_{\mathbf{e}, \mathbf{d}, \mathbf{m}}(\mathbf{v}) = \rho_{\mathbf{e}}(v_{\mathbf{e}}) \rho_{\mathbf{d}}(v_{\mathbf{d}}) \rho_{\mathbf{m}}(v_{\mathbf{m}})$ with respect to a KR transport map \mathcal{T} . Using properties of conditional probability distributions and Bayes’ law,

$$(3.6) \quad \pi_{\mathbf{e}, \mathbf{d}, \mathbf{m}}(\mathbf{e}, \mathbf{d}, \mathbf{m}) = \pi_{\mathbf{d}|\mathbf{e}, \mathbf{m}}(\mathbf{d} | \mathbf{e}, \mathbf{m}) \pi_{\mathbf{m}}(\mathbf{m}) \pi_{\mathbf{e}}(\mathbf{e}),$$

where $\pi_{\mathbf{d}|\mathbf{e}, \mathbf{m}}$ is the design-dependent likelihood, $\pi_{\mathbf{m}}$ is the prior, $\pi_{\mathbf{e}}$ is a user-specified density for the design parameters \mathbf{e} , and $z > 0$ is a normalization constant. For the remainder of this section, we assume that such a map is available and define $\hat{\pi}_{\mathbf{e}, \mathbf{d}, \mathbf{m}} := \mathcal{T}_{\#} \rho_{\mathbf{e}, \mathbf{d}, \mathbf{m}}$ to be the approximation to the target density $\pi_{\mathbf{e}, \mathbf{d}, \mathbf{m}}$.

Remark 3.1 (On the probability density for the designs). *We note that the marginal density on the designs $\pi_{\mathbf{e}}$ is introduced as a consequence of the decomposition of the joint density $\pi_{\mathbf{e}, \mathbf{d}, \mathbf{m}}$ into the product of conditional marginal densities. In general, there is no single “correct” fixed choice for $\pi_{\mathbf{e}}$. In particular, under our assumptions on the likelihood and prior, the posterior density is independent of the particular choice for $\pi_{\mathbf{e}}$. We defer making any specific choices to Section 6. It is important, however, that the support of $\pi_{\mathbf{e}}$ covers the space of possible designs \mathcal{E} and we assume this henceforth. Additionally, while the posterior is unchanged for different choices of $\pi_{\mathbf{e}}$, it does of course change the joint density.*

The Knothe-Rosenblatt rearrangement for an arbitrary law on the random variables $\mathbf{x} = (x_1, \dots, x_n)$ is unique once a particular arrangement of the variables is prescribed. While there are advantages to other arrangements of the variables (including ease of computation), we order the design, observable

and inference parameter random variables as $\mathbf{x} = (\mathbf{e}, \mathbf{d}, \mathbf{m})$. The triangular KR map \mathcal{T} is then defined component-wise; analogously to (3.5), i.e.,

$$(3.7) \quad \mathcal{T}(\mathbf{v}) := \mathcal{T}(\mathbf{v}_e, \mathbf{v}_d, \mathbf{v}_m) = \begin{bmatrix} \mathcal{T}_e(\mathbf{v}_e) \\ \mathcal{T}_{d|e}(\mathbf{v}_e, \mathbf{v}_d) \\ \mathcal{T}_{m|e,d}(\mathbf{v}_e, \mathbf{v}_d, \mathbf{v}_m) \end{bmatrix} = \begin{bmatrix} \mathbf{e} \\ \mathbf{d} \\ \mathbf{m} \end{bmatrix} = \mathbf{x}.$$

The main advantage of using this particular arrangement over alternative orderings is the immediate access to the conditional distributions needed for defining the OED optimality criteria.

Specifically, as described in Section 3.1, for any fixed $\mathbf{e}^* \in \mathbb{R}^{n_e}$ and $\mathbf{d}^* \in \mathbb{R}^{n_d}$, couplings between the approximate evidence density $\hat{\pi}_{d|e^*} \approx \pi_{d|e^*}$ and the marginal reference ρ_d as well as the approximate posterior density $\hat{\pi}_{m|e^*,d^*} \approx \pi_{m|e^*,d^*}$ and the marginal reference ρ_m can be defined through the operators $\mathcal{T}^{e^*}: \mathbb{R}^{n_d} \rightarrow \mathbb{R}^{n_d}$ and $\mathcal{T}^{e^*,d^*}: \mathbb{R}^{n_m} \rightarrow \mathbb{R}^{n_m}$ as follows:

$$(3.8) \quad \begin{aligned} \mathbf{v}_d \sim \rho_d &\Rightarrow \mathcal{T}^{e^*}(\mathbf{v}_d) := \mathcal{T}_{d|e}(\mathbf{v}_e^*, \mathbf{v}_d) \sim \hat{\pi}_{d|e^*}, \\ \mathbf{v}_m \sim \rho_m &\Rightarrow \mathcal{T}^{e^*,d^*}(\mathbf{v}_m) := \mathcal{T}_{m|e,d}(\mathbf{v}_e^*, \mathbf{v}_d^*, \mathbf{v}_m) \sim \hat{\pi}_{m|e^*,d^*}, \end{aligned}$$

where $\mathbf{v}_e^* := \mathcal{T}_e^{-1}(\mathbf{e}^*)$ and $\mathbf{v}_d^* := \mathcal{T}_{d|e}^{-1}(\mathbf{e}^*, \mathbf{d}^*)$; in the latter the inverse is taken w.r.t. the data variable \mathbf{d} .

3.3. Approximation of optimality criteria using KR maps. Recall that our OED objective is to find a design $\mathbf{e}^* \in \mathcal{E}$ that maximizes an expected utility function Ψ ,

$$\mathbf{e}^* \in \underset{\mathbf{e} \in \mathcal{E}}{\text{Arg max}} \Psi(\mathbf{e}) = \underset{\mathbf{e} \in \mathcal{E}}{\text{Arg max}} \mathbb{E}_{\pi_{d|e}} [\psi(\mathbf{e}, \mathbf{d})].$$

The most evident way to make use of the transport-map-based surrogate for the joint density $\pi_{e,d,m}$ is a direct replacement of all the conditional densities in Ψ with their corresponding transport-map-based surrogates. The resulting approximate optimality criterion $\hat{\Psi}$ can then be approximated using Monte Carlo or Quasi-Monte Carlo quadrature.

This approach could be used for a wide variety of optimality criteria. Let $\hat{\psi}$ denote a problem-dependent approximation to the utility function ψ and assume $\mathbf{v}_d^{(i)} \sim \rho_d$. Using (3.4), the procedure for an arbitrary utility function can be summarized with the following sequence of approximations:

$$\Psi(\mathbf{e}) \approx \underbrace{\mathbb{E}_{\hat{\pi}_{d|e}} [\hat{\psi}(\mathbf{e}, \mathbf{d})]}_{=:\hat{\Psi}(\mathbf{e})} = \underbrace{\mathbb{E}_{\rho_d} [\hat{\psi}(\mathbf{e}, \mathcal{T}^e(\mathbf{v}_d))]}_{=:\hat{\Psi}^N(\mathbf{e})} \approx \frac{1}{N} \sum_{i=1}^N \hat{\psi}(\mathbf{e}, \mathcal{T}^e(\mathbf{v}_d^{(i)})).$$

However, in the results presented in Section 6, we focus on the commonly-used A- and D-optimal design objectives. Hence, we specify the exact procedure used for approximating those two objectives.

A-Optimal design. We propose the following approximation to the A-optimal objective for any $\mathbf{e} \in \mathcal{E}$:

$$(3.9) \quad \begin{aligned} \Psi_A(\mathbf{e}) &= -\mathbb{E}_{\pi_{d|e}} [\text{trace}(\mathbf{C}_{m|e,d}(\mathbf{e}, \mathbf{d}))] \approx -\mathbb{E}_{\hat{\pi}_{d|e}} [\text{trace}(\hat{\mathbf{C}}_{m|e,d}(\mathbf{e}, \mathbf{d}))] =: \hat{\Psi}_A(\mathbf{e}) \\ &\approx -\frac{1}{N} \sum_{i=1}^N \text{trace}(\hat{\mathbf{C}}_{m|e,d^{(i)}}(\mathbf{e}, \mathbf{d}^{(i)})) =: \hat{\Psi}_A^N(\mathbf{e}). \end{aligned}$$

Here, $\{\mathbf{d}^{(i)}\}_{i=1}^N$ are data samples from the approximate evidence, $\mathbf{d}^{(i)} \sim \hat{\pi}_{d|e}$, and the covariance matrix for each data sample $\mathbf{C}_{m|e,d^{(i)}}$ is approximated via a sample average as

$$\mathbf{C}_{m|e,d^{(i)}}(\mathbf{e}, \mathbf{d}^{(i)}) \approx \hat{\mathbf{C}}_{m|e,d^{(i)}}(\mathbf{e}, \mathbf{d}^{(i)}) := \frac{1}{M-1} \sum_{k=1}^M (\mathbf{m}^{(k,i)} - \bar{\mathbf{m}}^{(i)}) (\mathbf{m}^{(k,i)} - \bar{\mathbf{m}}^{(i)})^T$$

with $\mathbf{m}^{(k,i)} \sim \hat{\pi}_{m|e,d^{(i)}}$ and $\bar{\mathbf{m}}^{(i)} := \frac{1}{M} \sum_{k=1}^M \mathbf{m}^{(k,i)}$. The samples $\mathbf{d}^{(i)}$ and $\mathbf{m}^{(k,i)}$ are obtained using the transport map \mathcal{T} as described in (3.8). The full procedure for evaluating $\hat{\Psi}_A^N(\mathbf{e})$ for any design $\mathbf{e} \in \mathcal{E}$ is summarized in Algorithm 1.

Algorithm 1 Evaluate $\hat{\Psi}_A^N(e) \approx \Psi_A(e)$ using transport map to joint density.

```

1: procedure AOPT( $\rho_{e,d,m}, \mathcal{T}, e, N, M$ )                                     #  $\mathcal{T}_\# \rho_{e,d,m} \approx \pi_{e,d,m}$ 
2:   Sample  $v_d^{(i)} \sim \rho_d$  for  $i = 1, \dots, N$ ,  $v_m^{(k)} \sim \rho_m$  for  $k = 1, \dots, M$ 
3:    $d^{(i)} \leftarrow \mathcal{T}^e(v_d^{(i)})$  for  $i = 1, \dots, N$                                      # Equation (3.8)
4:   for  $i=1, \dots, N$  do
5:      $m^{(k,i)} \leftarrow \mathcal{T}^{e,d^{(i)}}(v_m^{(k)})$  for  $k = 1, \dots, M$                        # Equation (3.8)
6:      $\bar{m}^{(i)} \leftarrow \frac{1}{M} \sum_{k=1}^M m^{(k,i)}$ 
7:      $\hat{C}_{m|e,d^{(i)}}(e, d^{(i)}) \leftarrow \frac{1}{M-1} \sum_{k=1}^M (m^{(k,i)} - \bar{m}^{(i)})(m^{(k,i)} - \bar{m}^{(i)})^T$ 
8:   end for
9:    $\hat{\Psi}_A^N \leftarrow \frac{1}{N} \sum_{i=1}^N \text{trace}[\hat{C}_{m|e,d^{(i)}}(e, d^{(i)})]$ 
10:  return  $\hat{\Psi}_A^N(e)$ 
11: end procedure

```

D-Optimal design. Similarly, we propose the following approximation to the expected information gain (EIG):

$$\begin{aligned}
 \Psi_D(e) &= \mathbb{E}_{\pi_{d,m|e}} \left[\log \left(\frac{\pi_{m|e,d}}{\pi_m} \right) \right] \approx \mathbb{E}_{\hat{\pi}_{d,m|e}} \left[\log \left(\frac{\hat{\pi}_{m|e,d}}{\pi_m} \right) \right] =: \hat{\Psi}_D(e) \\
 (3.10) \quad &\approx \frac{1}{N} \sum_{i=1}^N \log \left(\frac{\hat{\pi}_{m|e,d}(m^{(i)} | e, d^{(i)})}{\pi_m(m^{(i)})} \right) =: \hat{\Psi}_D^N(e).
 \end{aligned}$$

Here, joint samples $(d^{(i)}, m^{(i)}) \sim \hat{\pi}_{d,m|e}$ are obtained by transforming $(v_d, v_m) \sim \rho_{d,m}$ using the transport map \mathcal{T} and (3.8). Algorithm 2 summarizes the procedure for evaluating $\hat{\Psi}_D^N(e)$ for any $e \in \mathcal{E}$.

Algorithm 2 Evaluate $\hat{\Psi}_D^N(e) \approx \Psi_D(e)$ using transport map to joint density.

```

1: procedure DOPT( $\rho_{e,d,m}, \mathcal{T}, \pi_m, e, N$ )                                     #  $\mathcal{T}_\# \rho_{e,d,m} \approx \pi_{e,d,m}$ 
2:   Sample  $(v_d^{(i)}, v_m^{(i)}) \sim \rho_{d,m}$  for  $i = 1, \dots, N$ 
3:    $(d^{(i)}, m^{(i)}) \leftarrow (\mathcal{T}^e(v_d^{(i)}), \mathcal{T}^{e,d^{(i)}}(v_m^{(i)}))$  for  $i = 1, \dots, N$        # Equation (3.8)
4:   for  $i=1, \dots, N$  do
5:      $\hat{\pi}_{m|e,d^{(i)}}(m^{(i)}) = (\mathcal{T}^{e,d^{(i)}})_\# \rho_m(m^{(i)})$                                #  $\mathcal{T}^{e,d^{(i)}}$  defined in (3.8)
6:      $\psi_D(e, d^{(i)}, m^{(i)}) \leftarrow \log \left( \frac{\hat{\pi}_{m|e,d^{(i)}}(m^{(i)})}{\pi_m(m^{(i)})} \right)$ 
7:   end for
8:    $\hat{\Psi}_D^N(e) \leftarrow \frac{1}{N} \sum_{i=1}^N \psi_D(e, d^{(i)}, m^{(i)})$ 
9:   return  $\hat{\Psi}_D^N(e)$ 
10: end procedure

```

With these Monte Carlo approximations to Ψ_X (for $X = A, D$), the OED goal reduces to finding a design vector e^* that maximizes the tractable approximate expected utility function

$$(3.11) \quad e^* \in \underset{e \in \mathcal{E}}{\text{Arg max}} \hat{\Psi}_X^N(e).$$

A detailed discussion of viable algorithms for optimizing $\hat{\Psi}_X^N$ is outside the scope of this work. For the numerical results in Section 6, we use gradient-free optimization that do not require of $\hat{\Psi}_X^N$. Of course, gradient-based optimizers can also be used, provided $\hat{\Psi}_X^N(e)$ is differentiable with respect to e . This choice is left to be a black box to be specified by the user.

3.4. Error estimates for the transport-based approximations of expected information gain.

In the following, we derive probabilistic bounds for the error due to approximating the D-optimality criterion Ψ_D by the corresponding transport-map-based surrogate $\hat{\Psi}_D$ defined in (3.10). That is, for any $\zeta > 0$, we provide a lower bound for

$$(3.12) \quad \mathbb{P}_{\pi_e} \left[|\Psi_D(e) - \hat{\Psi}_D(e)| \leq \zeta \right],$$

where $|\Psi_D(e) - \hat{\Psi}_D(e)| := |\mathbb{E}_{\pi_{d,m|e}}[h] - \mathbb{E}_{\hat{\pi}_{d,m|e}}[\hat{h}]|$ with

$$(3.13) \quad h(e, \mathbf{d}, \mathbf{m}) := \log \left(\frac{\pi_{\mathbf{m}|e, \mathbf{d}}}{\pi_{\mathbf{m}}} \right) \quad \text{and} \quad \hat{h}(e, \mathbf{d}, \mathbf{m}) := \log \left(\frac{\hat{\pi}_{\mathbf{m}|e, \mathbf{d}}}{\pi_{\mathbf{m}}} \right).$$

We focus on the D-optimality criterion here for illustrative purposes. Bounds for the A-optimality criterion can be derived similarly.

The error estimates we derive depend on the Hellinger distance between the target and surrogate densities $\pi_{e, \mathbf{d}, \mathbf{m}}$ and $\hat{\pi}_{e, \mathbf{d}, \mathbf{m}}$:

$$(3.14) \quad \mathcal{D}_H(\pi_{e, \mathbf{d}, \mathbf{m}}, \hat{\pi}_{e, \mathbf{d}, \mathbf{m}}) := \left(\frac{1}{2} \int \left(\sqrt{\hat{\pi}_{e, \mathbf{d}, \mathbf{m}}} - \sqrt{\pi_{e, \mathbf{d}, \mathbf{m}}} \right)^2 d\mathbf{d} d\mathbf{m} \right)^{\frac{1}{2}}.$$

As shown in Section 4, this choice is particularly useful for tensor-train-based approximations to the transport maps, since the resulting surrogates naturally satisfy $\mathcal{D}_H(\pi_{e, \mathbf{d}, \mathbf{m}}, \hat{\pi}_{e, \mathbf{d}, \mathbf{m}}) \leq \varepsilon$, for some $\varepsilon \geq 0$. However, alternative constructions using other statistical distances/divergences, e.g., $\mathcal{D}_{KL}(\pi_{e, \mathbf{d}, \mathbf{m}} \| \hat{\pi}_{e, \mathbf{d}, \mathbf{m}})$ may lead to potentially sharper error estimates using other notions of distance or divergence.

To derive the lower bound, we make use of the following lemmas, the first two of which concerns arbitrary PDFs of a random variable \mathbf{x} taking values in $\mathcal{X} \subseteq \mathbb{R}^{n_x}$ for some $n_x \in \mathbb{N}$. To ease readability, we let

$$L_\pi^2(\mathcal{X}) := \{h: \mathcal{X} \rightarrow \mathbb{R} \mid h \text{ is measurable and } \|h\|_{L_\pi^2} < \infty\}$$

where

$$\|h\|_{L_\pi^2} := \sqrt{\mathbb{E}_\pi[h^2]}.$$

Lemma 3.2 ([20, Proposition 6]). *Let π and $\hat{\pi}$ be two PDFs. For any function $h \in L_\pi^2(\mathcal{X}) \cap L_{\hat{\pi}}^2(\mathcal{X})$,*

$$(3.15) \quad |\mathbb{E}_\pi[h] - \mathbb{E}_{\hat{\pi}}[h]| \leq \sqrt{2} \mathcal{D}_H(\pi, \hat{\pi}) \left(\|h\|_{L_\pi^2} + \|h\|_{L_{\hat{\pi}}^2} \right).$$

Lemma 3.3. *Let the ratio of two PDFs π and $\hat{\pi}$ be bounded from above almost surely, i. e.,*

$$(3.16) \quad \sup_{\mathbf{x} \in \mathcal{X} \subseteq \mathbb{R}^{n_x}} \frac{\pi(\mathbf{x})}{\hat{\pi}(\mathbf{x})} \leq c < \infty.$$

Then the KL divergence of π from $\hat{\pi}$ can be bounded as follows:

$$(3.17) \quad \mathcal{D}_{KL}(\pi \| \hat{\pi}) \leq \sqrt{2} \mathcal{D}_H(\pi, \hat{\pi}) \left(\left\| \frac{\pi}{\hat{\pi}} \right\|_{L_\pi^2} + \left\| \frac{\pi}{\hat{\pi}} \right\|_{L_{\hat{\pi}}^2} \right).$$

Proof. Under our assumptions, using [30, Theorem 5], $\mathcal{D}_{KL}(\pi \| \hat{\pi}) \leq \mathcal{D}_{\chi^2}(\pi \| \hat{\pi})$ where $\mathcal{D}_{\chi^2}(\pi \| \hat{\pi})$ denotes the χ^2 -divergence of π from $\hat{\pi}$. The statement then follows from [20, Corollary 2]. \square

Now, consider two probability densities $\pi_{\mathbf{x}, \mathbf{y}} = \pi_{\mathbf{x}|\mathbf{y}} \pi_{\mathbf{y}}$ and $\hat{\pi}_{\mathbf{x}, \mathbf{y}} = \hat{\pi}_{\mathbf{x}|\mathbf{y}} \hat{\pi}_{\mathbf{y}}$ defined on the product space $\mathcal{X} \times \mathcal{Y} \subseteq \mathbb{R}^{n_x} \times \mathbb{R}^{n_y}$ (with $n_x, n_y \in \mathbb{N}$).

Lemma 3.4 ([21, Lemma 4]). *The expected value of the Hellinger distance between $\pi_{\mathbf{x}|\mathbf{y}}$ and $\hat{\pi}_{\mathbf{x}|\mathbf{y}}$ satisfies:*

$$(3.18) \quad \mathbb{E}_{\pi_{\mathbf{y}}} \left[\mathcal{D}_H(\pi_{\mathbf{x}|\mathbf{y}}, \hat{\pi}_{\mathbf{x}|\mathbf{y}}) \right] \leq 2 \mathcal{D}_H(\pi_{\mathbf{x}, \mathbf{y}}, \hat{\pi}_{\mathbf{x}, \mathbf{y}}).$$

Furthermore,

$$(3.19) \quad \mathbb{E}_{\pi_{\mathbf{y}}} \left[\mathcal{D}_H(\pi_{\mathbf{x}|\mathbf{y}}, \hat{\pi}_{\mathbf{x}|\mathbf{y}})^2 \right] \leq 4 \mathcal{D}_H(\pi_{\mathbf{x}, \mathbf{y}}, \hat{\pi}_{\mathbf{x}, \mathbf{y}})^2.$$

Proposition 3.5. Assume the PDFs $\pi_{\mathbf{x},\mathbf{y}}$ and $\hat{\pi}_{\mathbf{x},\mathbf{y}}$ satisfy $\mathcal{D}_H(\pi_{\mathbf{x},\mathbf{y}}, \hat{\pi}_{\mathbf{x},\mathbf{y}}) \leq \varepsilon$ for some $\varepsilon \geq 0$. Furthermore, assume that the ratio of the conditional densities $\pi_{\mathbf{x}|\mathbf{y}}$ and $\hat{\pi}_{\mathbf{x}|\mathbf{y}}$ is bounded almost surely by $c_1 \in L^2_{\pi_{\mathbf{y}}}(\mathcal{Y})$, i. e., for all $\mathbf{y} \in \mathcal{Y}$,

$$(3.20) \quad \sup_{\mathbf{x} \in \mathcal{X}} \frac{\pi_{\mathbf{x}|\mathbf{y}}(\mathbf{x})}{\hat{\pi}_{\mathbf{x}|\mathbf{y}}(\mathbf{x})} \leq c_1(\mathbf{y}).$$

Then we have the following bound on the expected error:

$$(3.21) \quad \mathbb{E}_{\pi_{\mathbf{x},\mathbf{y}}} \left[\log \left(\frac{\pi_{\mathbf{x}|\mathbf{y}}}{\hat{\pi}_{\mathbf{x}|\mathbf{y}}} \right) \right] \leq 4 \sqrt{2} \varepsilon \|c_1\|_{L^2_{\pi_{\mathbf{y}}}}.$$

Proof. Note that

$$\begin{aligned} \mathbb{E}_{\pi_{\mathbf{x},\mathbf{y}}} \left[\log \left(\frac{\pi_{\mathbf{x}|\mathbf{y}}}{\hat{\pi}_{\mathbf{x}|\mathbf{y}}} \right) \right] &= \mathbb{E}_{\pi_{\mathbf{y}}} \left[\mathbb{E}_{\pi_{\mathbf{x}|\mathbf{y}}} \left[\log \left(\frac{\pi_{\mathbf{x}|\mathbf{y}}}{\hat{\pi}_{\mathbf{x}|\mathbf{y}}} \right) \right] \right] \\ &= \mathbb{E}_{\pi_{\mathbf{y}}} [\mathcal{D}_{\text{KL}}(\pi_{\mathbf{x}|\mathbf{y}} \parallel \hat{\pi}_{\mathbf{x}|\mathbf{y}})] \leq 2 \sqrt{2} \mathbb{E}_{\pi_{\mathbf{y}}} [c_1(\mathbf{y}) \mathcal{D}_H(\pi_{\mathbf{x}|\mathbf{y}}, \hat{\pi}_{\mathbf{x}|\mathbf{y}})], \end{aligned}$$

where the inequality follows from Lemma 3.3 and assumption (3.20). Then, using Hölder's inequality and Lemma 3.4, we have

$$\mathbb{E}_{\pi_{\mathbf{y}}} [c_1(\mathbf{y}) \mathcal{D}_H(\pi_{\mathbf{x}|\mathbf{y}}, \hat{\pi}_{\mathbf{x}|\mathbf{y}})] \leq 2 \mathcal{D}_H(\pi_{\mathbf{x},\mathbf{y}}, \hat{\pi}_{\mathbf{x},\mathbf{y}}) \|c_1\|_{L^2_{\pi_{\mathbf{y}}}},$$

and the result (3.21) thus follows. \square

Proposition 3.6. Let $\pi_{\mathbf{x},\mathbf{y}}$ and $\hat{\pi}_{\mathbf{x},\mathbf{y}}$ be two PDFs satisfying $\mathcal{D}_H(\pi_{\mathbf{x},\mathbf{y}}, \hat{\pi}_{\mathbf{x},\mathbf{y}}) \leq \varepsilon$ for some $\varepsilon \geq 0$. Assume that the function $\hat{h}(\mathbf{y}, \cdot)$ is bounded almost surely from above by $c_2(\mathbf{y})$ with $c_2 \in L^2_{\pi_{\mathbf{y}}}(\mathcal{Y})$, i. e.,

$$(3.22) \quad \sup_{\mathbf{x} \in \mathcal{X}} |\hat{h}(\mathbf{y}, \mathbf{x})| \leq c_2(\mathbf{y}), \quad \text{for all } \mathbf{y} \in \mathcal{Y}.$$

Then

$$(3.23) \quad \mathbb{E}_{\pi_{\mathbf{y}}} \left[|\mathbb{E}_{\pi_{\mathbf{x}|\mathbf{y}}}[\hat{h}] - \mathbb{E}_{\hat{\pi}_{\mathbf{x}|\mathbf{y}}}[\hat{h}]| \right] \leq 4 \sqrt{2} \varepsilon \|c_2\|_{L^2_{\pi_{\mathbf{y}}}}.$$

Proof. Using Lemma 3.2, we have that

$$\mathbb{E}_{\pi_{\mathbf{y}}} \left[|\mathbb{E}_{\pi_{\mathbf{x}|\mathbf{y}}}[\hat{h}] - \mathbb{E}_{\hat{\pi}_{\mathbf{x}|\mathbf{y}}}[\hat{h}]| \right] \leq \mathbb{E}_{\pi_{\mathbf{y}}} \left[\sqrt{2} \mathcal{D}_H(\pi_{\mathbf{x}|\mathbf{y}}, \hat{\pi}_{\mathbf{x}|\mathbf{y}}) \left(\|\hat{h}\|_{L^2_{\pi_{\mathbf{x}|\mathbf{y}}}} + \|\hat{h}\|_{L^2_{\hat{\pi}_{\mathbf{x}|\mathbf{y}}}} \right) \right].$$

The result then follows from (3.22), Lemma 3.4, and Hölder's inequality. \square

Now we are ready to prove the main result of this section, which is a probabilistic bound for the error induced by the use of a transport-map-based approximation to the D-optimality criterion.

Theorem 3.7. Let $\pi_{\mathbf{e},\mathbf{d},\mathbf{m}}$ be the joint density for the design (\mathbf{e}), observable (\mathbf{d}), and inference parameters (\mathbf{m}), as defined in Section 3.2. Let $\hat{\pi}_{\mathbf{e},\mathbf{d},\mathbf{m}}$ be some approximation to $\pi_{\mathbf{e},\mathbf{d},\mathbf{m}}$ with $\mathcal{D}_H(\pi_{\mathbf{e},\mathbf{d},\mathbf{m}}, \hat{\pi}_{\mathbf{e},\mathbf{d},\mathbf{m}}) \leq \varepsilon$ for some $\varepsilon \geq 0$. Furthermore, for all $\mathbf{e} \in \mathcal{E}$ and $\mathbf{d} \in \mathcal{D}$, assume

$$(3.24) \quad \sup_{\mathbf{m} \in \mathcal{M}} \frac{\pi_{\mathbf{m}|\mathbf{e},\mathbf{d}}(\mathbf{m})}{\hat{\pi}_{\mathbf{m}|\mathbf{e},\mathbf{d}}(\mathbf{m})} \leq c_1(\mathbf{e}, \mathbf{d}) \quad \text{for all } (\mathbf{e}, \mathbf{d}) \in \mathcal{E} \times \mathcal{D} \text{ and}$$

$$(3.25) \quad \sup_{(\mathbf{d}, \mathbf{m}) \in \mathcal{D} \times \mathcal{M}} \left| \log \left(\frac{\hat{\pi}_{\mathbf{m}|\mathbf{e},\mathbf{d}}(\mathbf{m})}{\pi_{\mathbf{m}}(\mathbf{m})} \right) \right| \leq c_2(\mathbf{e}) \quad \text{for all } \mathbf{e} \in \mathcal{E}$$

for some $c_1 \in L^2_{\pi_{\mathbf{e},\mathbf{d}}}(\mathcal{E} \times \mathcal{D})$ and $c_2 \in L^2_{\pi_{\mathbf{e}}}(\mathcal{E})$ (with the spaces \mathcal{E} and \mathcal{D} as defined as in Section 2). Then,

$$(3.26) \quad \mathbb{E}_{\pi_{\mathbf{e}}} \left[|\Psi_D(\mathbf{e}) - \hat{\Psi}_D(\mathbf{e})| \right] \leq 4 \sqrt{2} \varepsilon \left(\|c_1\|_{L^2_{\pi_{\mathbf{e},\mathbf{d}}}} + \|\hat{c}_2\|_{L^2_{\pi_{\mathbf{e}}}} \right).$$

Additionally, for any $\zeta > 0$,

$$(3.27) \quad \mathbb{P}_{\pi_{\mathbf{e}}} \left[|\Psi_D(\mathbf{e}) - \hat{\Psi}_D(\mathbf{e})| \leq \zeta \right] \geq 1 - \frac{4 \sqrt{2} \varepsilon}{\zeta} \left(\|c_1\|_{L^2_{\pi_{\mathbf{e},\mathbf{d}}}} + \|\hat{c}_2\|_{L^2_{\pi_{\mathbf{e}}}} \right).$$

Proof. Let $h(\mathbf{e}, \mathbf{d}, \mathbf{m}) := \log\left(\frac{\pi_{\mathbf{m}|\mathbf{e},\mathbf{d}}}{\pi_{\mathbf{m}}}\right)$ and $\hat{h}(\mathbf{e}, \mathbf{d}, \mathbf{m}) := \log\left(\frac{\hat{\pi}_{\mathbf{m}|\mathbf{e},\mathbf{d}}}{\pi_{\mathbf{m}}}\right)$. By the triangle inequality, we have:

$$\begin{aligned} \mathbb{E}_{\pi_{\mathbf{e}}} \left[\left| \Psi_D(\mathbf{e}) - \hat{\Psi}_D(\mathbf{e}) \right| \right] &= \mathbb{E}_{\pi_{\mathbf{e}}} \left[\left| \mathbb{E}_{\pi_{\mathbf{d},\mathbf{m}|\mathbf{e}}} [h] - \mathbb{E}_{\hat{\pi}_{\mathbf{d},\mathbf{m}|\mathbf{e}}} [\hat{h}] \right| \right] \\ &\leq \mathbb{E}_{\pi_{\mathbf{e}}} \left[\left| \mathbb{E}_{\pi_{\mathbf{d},\mathbf{m}|\mathbf{e}}} [h - \hat{h}] \right| \right] + \mathbb{E}_{\pi_{\mathbf{e}}} \left[\left| \mathbb{E}_{\pi_{\mathbf{d},\mathbf{m}|\mathbf{e}}} [\hat{h}] - \mathbb{E}_{\hat{\pi}_{\mathbf{d},\mathbf{m}|\mathbf{e}}} [\hat{h}] \right| \right] \\ &= \mathbb{E}_{\pi_{\mathbf{e},\mathbf{d},\mathbf{m}}} \left[\log\left(\frac{\pi_{\mathbf{m}|\mathbf{e},\mathbf{d}}}{\hat{\pi}_{\mathbf{m}|\mathbf{e},\mathbf{d}}}\right) \right] + \mathbb{E}_{\pi_{\mathbf{e}}} \left[\left| \mathbb{E}_{\pi_{\mathbf{d},\mathbf{m}|\mathbf{e}}} [\hat{h}] - \mathbb{E}_{\hat{\pi}_{\mathbf{d},\mathbf{m}|\mathbf{e}}} [\hat{h}] \right| \right]. \end{aligned}$$

The first inequality (3.26) thus follows from Proposition 3.5 (with $\mathbf{x} = \mathbf{m}$ and $\mathbf{y} = (\mathbf{e}, \mathbf{d})$) and Proposition 3.6 (with $\mathbf{x} = (\mathbf{d}, \mathbf{m})$, $\mathbf{y} = \mathbf{e}$, and $\hat{h}(\mathbf{y}, \mathbf{x}) := \hat{h}(\mathbf{e}, \mathbf{d}, \mathbf{m}) = \log\left(\frac{\hat{\pi}_{\mathbf{m}|\mathbf{e},\mathbf{d}}}{\pi_{\mathbf{m}}}\right)$). The second statement (3.27) can be deduced by applying Markov's inequality. \square

Remark 3.8 (Some comments on the bounds and assumptions of Theorem 3.7.). *Note that for better readability, we make use of the constants $c_1(\mathbf{e}, \mathbf{d})$ and $c_2(\mathbf{e})$ to bound the expectations of $\frac{\pi_{\mathbf{m}|\mathbf{e},\mathbf{d}}}{\hat{\pi}_{\mathbf{m}|\mathbf{e},\mathbf{d}}}$ and $\log\left(\frac{\hat{\pi}_{\mathbf{m}|\mathbf{e},\mathbf{d}}}{\pi_{\mathbf{m}}}\right)$ respectively. Tighter upper bounds can be obtained by foregoing this simplification. Additionally, note that there is further error incurred due to the use of Monte Carlo approximation in the D-optimality criterion (3.10), i. e.,*

$$\mathbb{E}_{\pi_{\mathbf{e}}} \left[\left| \Psi_D(\mathbf{e}) - \hat{\Psi}_D^N(\mathbf{e}) \right| \right] \leq \mathbb{E}_{\pi_{\mathbf{e}}} \left[\left| \Psi_D(\mathbf{e}) - \hat{\Psi}_D(\mathbf{e}) \right| \right] + \mathbb{E}_{\pi_{\mathbf{e}}} \left[\left| \hat{\Psi}_D(\mathbf{e}) - \hat{\Psi}_D^N(\mathbf{e}) \right| \right].$$

However, $\mathbb{E}_{\pi_{\mathbf{e}}} \left[\left| \hat{\Psi}_D(\mathbf{e}) - \hat{\Psi}_D^N(\mathbf{e}) \right| \right]$ can be controlled by the sample size N .

4. CONSTRUCTION OF THE KNOTHE-ROSENBLATT REARRANGEMENT USING TENSOR TRAINS

In this section, we discuss an efficient numerical realization of the KR rearrangement (3.7). Building on [25, 20, 21], we construct the transport map via a functional tensor train (FTT) approximation to the square-root of the joint target density. We outline pertinent background material on FTTs in Section 4.1 and detail their utility in implementing the KR rearrangement in Section 4.2. Finally we present our FTT-based construction of the KR map approximating the joint density $\pi_{\mathbf{e},\mathbf{d},\mathbf{m}}$ and outline the corresponding OED algorithm in Section 4.3.

4.1. Functional tensor trains. The primary computational tool used in our approach is the functional tensor train decomposition [15, 31]. Given an arbitrary multivariate function $g: \mathcal{X} \rightarrow \mathbb{R}$ with $\mathcal{X} = \mathcal{X}_1 \times \mathcal{X}_2 \times \dots \times \mathcal{X}_n$, the FTT approximates $g(\mathbf{x})$ as the product of n univariate, matrix-valued functions $\mathbf{G}_k(x_k)$, i. e.,

$$(4.1) \quad g(\mathbf{x}) \approx \hat{g}(\mathbf{x}) := \mathbf{G}_1(x_1) \cdots \mathbf{G}_k(x_k) \cdots \mathbf{G}_n(x_n).$$

The functions $\mathbf{G}_k: \mathcal{X}_k \rightarrow \mathbb{R}^{r_{k-1} \times r_k}$ (with $r_0 = r_n = 1$) are commonly referred to as *TT cores* and the dimensions r_k are the corresponding *TT ranks*. Denoting by $\mathbf{A}_k \in \mathbb{R}^{r_{k-1} \times m_k \times r_k}$ a third-order coefficient tensor, the components of each \mathbf{G}_k can be represented as a linear combination of m_k basis functions $\{\phi_k^{(\ell)}\}_{\ell=1}^{m_k}$, i. e.,

$$(4.2) \quad [\mathbf{G}_k(x_k)]_{i,j} = \sum_{\ell=1}^{m_k} \phi_k^{(\ell)}(x_k) \mathbf{A}_k[i, \ell, j], \quad \text{for } i = 1, \dots, r_{k-1} \text{ and } j = 1, \dots, r_k.$$

The FTT decomposition can be built using efficient alternating-direction TT-cross approximation methods; for details see [46, 26]. We use a functional extension (described in [20, Appendix A] and [21, Appendix B]) of the rank-adaptive alternating minimal energy method in [26]. In general, the resulting decomposition only provides an approximation to the multivariate target function. However, given an error tolerance $\epsilon > 0$, this procedure adaptively chooses the TT ranks to minimize the L^2 residual error, resulting in an FTT approximation satisfying

$$(4.3) \quad \|g - \hat{g}\|_{L^2} := \left(\int_{\mathcal{X}} |g(\mathbf{x}) - \hat{g}(\mathbf{x})|^2 d\mathbf{x} \right)^{\frac{1}{2}} \leq \epsilon.$$

Introducing upper bounds on the ranks $r = \max_k r_k$ and on the number of basis functions $m = \max_k m_k$, the procedure constructs \hat{g} with $\mathcal{O}(nmr^2)$ evaluations of the function g and $\mathcal{O}(nmr^3)$ floating point operations (FLOPs). Thus, for problems where the function g is expensive to evaluate, the efficiency of the algorithm is highly dependent on the maximum ranks required to satisfy the ϵ error tolerance. The maximum rank typically depends on various properties of the function (smoothness, level of nonlinearity, dimension of \mathcal{X} , etc.), hence bounding the maximal rank for general functions is challenging. However, bounds have been established for some specific types of functions in [51, 32].

4.2. Construction of KR rearrangements via tensor train surrogates. Following [25, 20, 21, 56], we first outline the procedure for constructing the KR rearrangement in the general setting. Details of its application to design problems are given in the subsequent section. Specifically, here we consider the random variable $\mathbf{x} \in \mathcal{X} = \mathcal{X}_1 \times \dots \times \mathcal{X}_n$ with corresponding density

$$(4.4) \quad \pi_{\mathbf{x}}(\mathbf{x}) = \frac{p_{\mathbf{x}}(\mathbf{x})}{Z},$$

where $Z > 0$ is the normalizing constant. Throughout this section, we assume access to the *unnormalized* density $p_{\mathbf{x}}$ and treat Z as unknown.

Let $\rho_{\mathbf{x}}^{\text{UNIF}}$ be a uniform reference density defined on the unit hypercube $[0, 1]^n$. To construct a KR map, coupling $\rho_{\mathbf{x}}^{\text{UNIF}}$ and $\pi_{\mathbf{x}}$, we make use of the component notation $\mathbf{x}_{1:k} = [x_1, \dots, x_k]$, and let

$$\begin{aligned} F_{x_1}(x_1) &:= \int_{-\infty}^{x_1} \pi_{x_1}(x'_1) \, dx'_1, \\ F_{x_k|\mathbf{x}_{1:k-1}}(\mathbf{x}_{1:k}) &:= \int_{-\infty}^{x_k} \pi_{x_k|\mathbf{x}_{1:k-1}}(x'_k | \mathbf{x}_{1:k-1}) \, dx'_k = \int_{-\infty}^{x_k} \frac{\pi_{\mathbf{x}_{1:k}}(\mathbf{x}_{1:k-1}, x'_k)}{\pi_{\mathbf{x}_{1:k-1}}(\mathbf{x}_{1:k-1})} \, dx'_k \quad \text{for } k = 2, \dots, n, \end{aligned}$$

denote cumulative distribution functions (CDFs), where the marginal densities $\pi_{\mathbf{x}_{1:k}}$ (for $k = 1, \dots, n-1$) are given by

$$(4.5) \quad \pi_{\mathbf{x}_{1:k}}(\mathbf{x}_{1:k}) := \int_{\mathcal{X}_{>k}} \pi_{\mathbf{x}}(\mathbf{x}) \, d\mathbf{x}_{k+1:n}, \quad \mathcal{X}_{>k} := \mathcal{X}_{k+1} \times \dots \times \mathcal{X}_n.$$

Note that the map $\mathcal{S}: \mathcal{X} \rightarrow [0, 1]^n$, with

$$(4.6) \quad \mathcal{S}(\mathbf{x}) = \begin{bmatrix} F_{x_1}(x_1) \\ F_{x_2|x_1}(\mathbf{x}_{1:2}) \\ \vdots \\ F_{x_n|\mathbf{x}_{1:n-1}}(\mathbf{x}) \end{bmatrix} =: \mathbf{u},$$

defines a triangular order-preserving coupling (i.e., a KR rearrangement) between the uniform reference and the target, such that $\mathcal{S}_{\#} \pi_{\mathbf{x}} = \rho_{\mathbf{x}}^{\text{UNIF}}$. Through inversion of the map \mathcal{S} , we can define the map $\mathcal{T} \equiv \mathcal{S}^{-1}: [0, 1]^n \rightarrow \mathcal{X}$ that pushes forward the uniform reference to the target, $\mathcal{T}_{\#} \rho_{\mathbf{x}}^{\text{UNIF}} = \pi_{\mathbf{x}}$. Note that for any $\mathbf{u} \in [0, 1]^n$, the inverse map

$$(4.7) \quad \mathcal{T}(\mathbf{u}) := [F_{x_1}^{-1}(u_1), F_{x_2|x_1}^{-1}(\mathbf{u}_{1:2}), \dots, F_{x_n|\mathbf{x}_{1:n-1}}^{-1}(\mathbf{u})]^T$$

can be evaluated via a sequence of n inversions of scalar-valued functions. Specifically, $F_{x_k|\mathbf{x}_{1:k-1}}^{-1}(\mathbf{u}_{1:k})$ is evaluated by inverting $u_k = F_{x_k|\mathbf{x}_{1:k-1}}(\mathbf{x}_{1:k-1}, x_k)$ for x_k , where $\mathbf{x}_{1:k-1}$ is determined from the previous $k-1$ inversions. Thus, the key to realizing the KR map is the construction of the marginal densities $\pi_{\mathbf{x}_{1:k}}$ in (4.5) (and hence the CDFs).

In [20, 21, 56], the authors propose to construct these CDFs (and the map \mathcal{T}) via an FTT-based *approximation* to the joint density $\hat{\pi}_{\mathbf{x}} \approx \pi_{\mathbf{x}}$. To start, the square root of the unnormalized density is approximated using an FTT decomposition as described in Section 4.1, i.e., $\sqrt{p_{\mathbf{x}}(\mathbf{x})} \approx \hat{g}(\mathbf{x}) := \prod_{k=1}^n \mathbf{G}_k(x_k)$. In general, a rank-truncated TT approximation does not preserve non-negativity properties of the target function. Constructing the TT surrogate to the square root of the target density circumvents this challenge and ensures the approximate density function \hat{g}^2 is non-negative. The authors of [20, 56] further propose building a defensive approximation to the target density. Given a product-form reference density

$\rho_{\mathbf{x}}$ satisfying $\sup_{\mathbf{x}} \frac{p_{\mathbf{x}}(\mathbf{x})}{\rho_{\mathbf{x}}(\mathbf{x})} < \infty$ and a sufficiently small $\tau > 0$, the defensive FTT-based approximation to the target density is then given by

$$(4.8) \quad \hat{\pi}_{\mathbf{x}}(\mathbf{x}) = \frac{\hat{p}_{\mathbf{x}}(\mathbf{x})}{\hat{Z}}, \quad \hat{p}_{\mathbf{x}}(\mathbf{x}) = \hat{g}(\mathbf{x})^2 + \tau \rho_{\mathbf{x}}(\mathbf{x}),$$

where $\hat{Z} = \int \hat{p}_{\mathbf{x}}(\mathbf{x}) \, d\mathbf{x}$. This choice of approximation ensures $\sup_{\mathbf{x}} \frac{\pi_{\mathbf{x}}(\mathbf{x})}{\hat{\pi}_{\mathbf{x}}(\mathbf{x})} < \infty$, which is a crucial assumption for the error estimates derived in Section 3.4.

In addition to preserving non-negativity of the approximate density function, building an FTT to the square root of the target function via the rank-adaptive algorithm alluded to in Section 4.1 generates

$$\|\sqrt{p_{\mathbf{x}}} - \hat{g}\|_{L^2} \leq \epsilon$$

for some tolerance $\epsilon > 0$. As seen in Lemma 4.1, this bound naturally translates into a bound on the distance between the target density $\pi_{\mathbf{x}}$ and its TT-based surrogate $\hat{\pi}_{\mathbf{x}}$ (4.8).

Lemma 4.1 ([20, Proposition 4 and Theorem 1]). *Assume the L^2 error of the FTT approximation $\hat{g} \approx \sqrt{p_{\mathbf{x}}}$ is bounded, i. e., $\|\sqrt{p_{\mathbf{x}}} - \hat{g}\|_{L^2} \leq \epsilon$. Furthermore, assume $\tau \leq \epsilon^2$. Then, the Hellinger distance between $\hat{\pi}_{\mathbf{x}}$ defined in (4.8) and $\pi_{\mathbf{x}}$ in (4.4) satisfies:*

$$(4.9) \quad \mathcal{D}_{\text{H}}(\hat{\pi}_{\mathbf{x}}, \pi_{\mathbf{x}}) \leq \varepsilon := \frac{2\epsilon}{\sqrt{Z}}.$$

As discussed above, the FTT surrogate can be constructed at a cost of $\mathcal{O}(nmr^2)$ evaluations of $\sqrt{p_{\mathbf{x}}}$ and $\mathcal{O}(nmr^3)$ FLOPs. The approximate conditional PDFs, $\hat{\pi}_{x_j|\mathbf{x}_{1:j-1}} = \frac{\hat{\pi}_{\mathbf{x}_{1:j}}}{\hat{\pi}_{\mathbf{x}_{1:j-1}}}$, can then be expressed using the approximate marginal densities, which are defined as

$$(4.10) \quad \hat{\pi}_{\mathbf{x}_{1:k}}(\mathbf{x}_{1:k}) = \frac{1}{\hat{Z}} \left(\tau \rho_{\mathbf{x}_{1:k}}(\mathbf{x}_{1:k}) + \int_{\mathcal{X}_{>k}} \hat{g}(\mathbf{x})^2 \, d\mathbf{x}_{k+1:n} \right) \quad \text{for } k = 1, \dots, n-1,$$

where $\rho_{\mathbf{x}_{1:k}}(\mathbf{x}_{1:k}) := \prod_{i=1}^k \rho_{x_i}(x_i)$. As detailed in [21, Appendix B.3], the marginal densities in (4.10) can be computed analytically via a sequence of one-dimensional integrals, and the number of FLOPs required to construct these marginals, and hence the conditionals $\hat{\pi}_{x_j|\mathbf{x}_{1:j-1}}$, is $\mathcal{O}(nmr^3)$. The cost of evaluating the corresponding inverse map \mathcal{T} to transform a sample $\mathbf{u} \sim \rho_{\mathbf{x}}^{\text{UNIF}}$ to a sample $\mathbf{x} \sim \hat{\pi}_{\mathbf{x}} \approx \pi_{\mathbf{x}}$ in (4.7) requires $\mathcal{O}(nmr^2)$ FLOPs.

Finally, we note that the ability to construct a map \mathcal{S} between any target density $\pi_{\mathbf{x}}$ and the standard uniform reference $\rho_{\mathbf{x}}^{\text{UNIF}}$ is sufficient for constructing a Knothe-Rosenblatt transport between the joint density of interest $\pi_{\mathbf{x}}$ and any arbitrary product-form reference density $\rho_{\mathbf{x}}$. More precisely, given a diagonal map \mathcal{R} such that $\mathcal{R}_{\#} \rho_{\mathbf{x}} = \rho_{\mathbf{x}}^{\text{UNIF}}$, the composite map $\mathcal{T} = \mathcal{S}^{-1} \circ \mathcal{R}$ defines a lower-triangular map satisfying the property $\mathcal{T}_{\#} \rho_{\mathbf{x}} = \pi_{\mathbf{x}}$.

4.3. Construction of \mathcal{T} for OED using tensor trains and a deep composition of KR maps.

Recall our objective to construct a transport map \mathcal{T} of the form (3.7) to couple a product-form reference density $\rho_{\mathbf{e},\mathbf{d},\mathbf{m}}$ to an approximation $\hat{\pi}_{\mathbf{e},\mathbf{d},\mathbf{m}}$ of the joint density for the design, observable and inference parameter random variables. As in Section 3.2, the joint density $\pi_{\mathbf{e},\mathbf{d},\mathbf{m}} = \pi_{\mathbf{d}|\mathbf{e},\mathbf{m}} \pi_{\mathbf{m}} \pi_{\mathbf{e}}$, where $\pi_{\mathbf{d}|\mathbf{e},\mathbf{m}} \propto \exp(-\frac{1}{2} \|\mathcal{F}(\mathbf{e}, \mathbf{m}) - \mathbf{d}\|_{\Gamma_{\eta(\mathbf{e})}^{-1}}^2)$ is the likelihood with parameter-to-observable map \mathcal{F} , $\pi_{\mathbf{m}}$ is the prior, and $\pi_{\mathbf{e}}$ is a user-specified density for the design parameters. Again we let $\pi_{\mathbf{e},\mathbf{d},\mathbf{m}} = \frac{p_{\mathbf{e},\mathbf{d},\mathbf{m}}}{Z}$, assuming access only to the *unnormalized* joint density, $p_{\mathbf{e},\mathbf{d},\mathbf{m}}$, and treating the normalizing constant $Z > 0$ as unknown. These joint densities $\pi_{\mathbf{e},\mathbf{d},\mathbf{m}}$ tend to concentrate in some subdomain and exhibit complex nonlinear correlation structures, even in the relatively simple case of a linear parameter-to-observable map \mathcal{F} , additive Gaussian noise and Gaussian prior.

Example 4.2. *As an illustrative example, consider an inverse problem governed by Poisson's equation $-u_{xx} = m_1 \sin(\frac{4}{3}x) + m_2 \cos(2x)$ with constant Dirichlet data prescribed at the boundaries of the domain interval $\Omega := (0, 2\pi)$. The design problem is choosing the location $e \in \Omega$ where the state u should be measured to optimally infer the parameter $\mathbf{m} = [m_1, m_2]$. Despite the Gaussian likelihood and posterior,*

the joint density $\pi_{e,d}$ (visualized in Figure 4.1) is non-Gaussian even in this simple toy example. In particular, the density has multiple sharp peaks and concentrates along the diagonal.

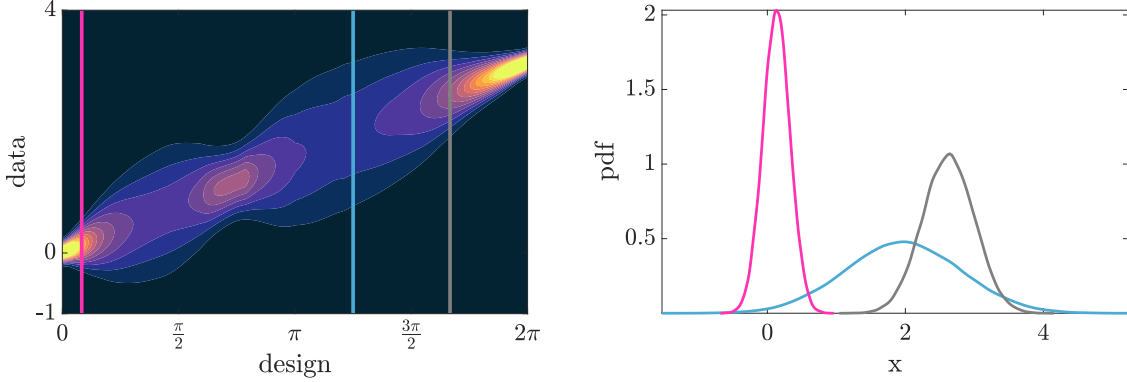


FIGURE 4.1. On the left, a contour plot of a two-dimensional density $\pi_{e,d}$ for the illustrative toy problem in Example 4.2. A visualization of $\pi_{d|e^*}$ for three different design locations e^* is visualized in the right image. The three different designs correspond to the vertical color-coded lines overlaid on the contour plot in the left.

In this situation, following the procedure outlined in Section 4.2 and constructing the transport map surrogate to $\sqrt{p_{e,d,m}}$ via FTT approximation in one step leads to very large ranks to ensure $\mathcal{D}_H(\hat{\pi}_{e,d,m}, \pi_{e,d,m}) \leq \varepsilon$ for suitably small error tolerances ε . Typically, the computational bottleneck of constructing the FTT decomposition for problems where the PTO map involves discretized PDE/ODE solves is the evaluation of the unnormalized density, since each evaluation requires solving the aforementioned PDE/ODE. The computational efficiency or feasibility to construct \mathcal{T} strongly depends on the ranks, since the required number of density evaluations scales quadratically with the rank. For certain problems this bottleneck could be mitigated by employing a reduced-order model surrogate to the parameter-to-observable map. However, a sufficiently accurate surrogate may not be available, or may still be rather expensive to evaluate. In general, keeping the ranks as small as possible while maintaining accuracy of the approximation is vital to the efficiency of the algorithm.

To alleviate the challenges presented by such complex densities, the authors of [20] propose the *deep inverse Rosenblatt transport* (DIRT), a procedure that builds a composition of transport maps guided by a suitable sequence of bridging densities. Let $\{p_{e,d,m}^\ell\}_{\ell=1}^L$ be a sequence of unnormalized bridging densities that gradually captures the complexity of the joint target density such that $p_{e,d,m}^L := p_{e,d,m}$ (see Remark 4.3 for some suitable choices). The full composite transport map \mathcal{T} to approximate $\mathcal{T}_\# \rho_{e,d,m} = \hat{\pi}_{e,d,m} \approx \pi_{e,d,m}$ is defined as

$$(4.11) \quad \mathcal{T} := \mathcal{T}_L = \mathcal{Q}_1 \circ \mathcal{Q}_2 \circ \dots \circ \mathcal{Q}_L.$$

For each layer ℓ , the composite transport map $\mathcal{T}_\ell = \mathcal{Q}_1 \circ \dots \circ \mathcal{Q}_\ell$ provides an approximation to the ℓ -th normalized bridging density $\pi_{e,d,m}^\ell = \frac{p_{e,d,m}^\ell}{Z^\ell}$, i.e., $(\mathcal{T}_\ell)_\# \rho_{e,d,m} = \hat{\pi}_{e,d,m}^\ell \approx \pi_{e,d,m}^\ell$. Here, $Z^\ell > 0$ is the normalizing constant of the ℓ -th bridging density.

The intermediate maps are constructed recursively. At stage $\ell + 1$, assuming \mathcal{T}_ℓ is built, the next layer $\mathcal{Q}_{\ell+1}$ is constructed as a squared inverse KR-map (using the procedure outlined in Section 4.2) satisfying $(\mathcal{Q}_{\ell+1})_\# \rho_{e,d,m} = q_{e,d,m}^{\ell+1} \approx \mathcal{T}_\ell^\# \pi_{e,d,m}^{\ell+1}$. This requires building an FTT approximation to the square root of the unnormalized intermediate density $q_{e,d,m}^{\ell+1}$. Using (3.3) as well as the property that $\mathcal{T}_\ell^\# \pi_{e,d,m}^\ell \approx \rho_{e,d,m}$, the intermediate density

$$(4.12) \quad q_{e,d,m}^{\ell+1}(\mathbf{u}) \approx \mathcal{T}_\ell^\# \pi_{e,d,m}^{\ell+1}(\mathbf{u}) = \frac{\pi_{e,d,m}^{\ell+1}(\mathcal{T}_\ell(\mathbf{u}))}{\pi_{e,d,m}^\ell(\mathcal{T}_\ell(\mathbf{u}))} \rho_{e,d,m}(\mathbf{u})$$

can be viewed as a perturbation of the reference density $\rho_{\mathbf{e}, \mathbf{d}, \mathbf{m}}$ by the ratio $\frac{\pi_{\mathbf{e}, \mathbf{d}, \mathbf{m}}^{\ell+1}(\mathcal{T}_\ell(\mathbf{u}))}{\pi_{\mathbf{e}, \mathbf{d}, \mathbf{m}}^\ell(\mathcal{T}_\ell(\mathbf{u}))}$. For suitably chosen bridging densities, $q_{\mathbf{e}, \mathbf{d}, \mathbf{m}}^{\ell+1}(\mathbf{u})$ will be less complicated and concentrated than the bridging density $\pi_{\mathbf{e}, \mathbf{d}, \mathbf{m}}^{\ell+1}$, and hence easier to approximate in the FTT format. This procedure can be seen as a successive change of coordinates or preconditioning procedure.

Since the Hellinger distance is invariant to changes in measure, the error in approximating the target $\pi_{\mathbf{e}, \mathbf{d}, \mathbf{m}}$ by the pushforward of $\rho_{\mathbf{e}, \mathbf{d}, \mathbf{m}}$ with respect to the final composite map $\mathcal{T}_L = \mathcal{T}_{L-1} \circ \mathcal{Q}_L$ is

$$(4.13) \quad \mathcal{D}_H((\mathcal{T}_{L-1} \circ \mathcal{Q}_L)_\# \rho_{\mathbf{e}, \mathbf{d}, \mathbf{m}}, \pi_{\mathbf{e}, \mathbf{d}, \mathbf{m}}) = \mathcal{D}_H((\mathcal{Q}_L)_\# \rho_{\mathbf{e}, \mathbf{d}, \mathbf{m}}, (\mathcal{T}_{L-1})^\# \pi_{\mathbf{e}, \mathbf{d}, \mathbf{m}}).$$

Thus, $\mathcal{D}_H(\hat{\pi}_{\mathbf{e}, \mathbf{d}, \mathbf{m}}, \pi_{\mathbf{e}, \mathbf{d}, \mathbf{m}})$ can be controlled by ensuring that the error in the last layer satisfies $\mathcal{D}_H((\mathcal{Q}_L)_\# \rho_{\mathbf{e}, \mathbf{d}, \mathbf{m}}, (\mathcal{T}_{L-1})^\# \pi_{\mathbf{e}, \mathbf{d}, \mathbf{m}}) \leq \varepsilon$ for some $\varepsilon \in (0, 1]$. This can be guaranteed by building a sufficiently accurate FTT approximation to the square root of the unnormalized pullback density $(\mathcal{T}_{L-1})^\# \pi_{\mathbf{e}, \mathbf{d}, \mathbf{m}}$ as described in [Lemma 4.1](#). We outline the DIRT procedure for constructing the transport map surrogate to $\pi_{\mathbf{e}, \mathbf{d}, \mathbf{m}}$ in [Algorithm 3](#). Once this transport map is constructed, it could be used to approximate the expected utility function exactly as described in [Section 3.3](#). In particular, we then present the DIRT-based algorithm for computing D- and A-optimal designs in [Algorithm 4](#).

Algorithm 3 Deep Inverse Rosenblatt Transport (DIRT) [20].

```

1: procedure DIRT( $\rho, p$ )                                # Constructs a map  $\mathcal{T}_L$  coupling reference  $\rho$  with target  $\pi = \frac{p}{z}$ 
2:   Choose bridging densities  $\{p_{\mathbf{e}, \mathbf{d}, \mathbf{m}}^\ell\}_{\ell=0}^L$                                      # See Remark 4.3
3:    $\hat{g}^1 \leftarrow$  FTT approx. to  $\sqrt{p^1}$ 
4:    $\mathcal{T}_1 \leftarrow$  squared inverse KR map satisfying  $(\mathcal{T}_1)_\# \rho \approx \pi^1 = \frac{p^1}{z^1}$            # As outlined in Section 4.2
5:   for  $\ell = 2, \dots, L$  do
6:      $\hat{g}^\ell \leftarrow$  FTT approx. to  $\sqrt{(\mathcal{T}_{\ell-1})^\# p^\ell}$ 
7:      $\mathcal{Q}_\ell \leftarrow$  inverse KR map satisfying  $(\mathcal{Q}_\ell)_\# \rho \approx \pi^\ell = \frac{p^\ell}{z^\ell}$            # As outlined in Section 4.2
8:      $\mathcal{T}_\ell \leftarrow \mathcal{T}_{\ell-1} \circ \mathcal{Q}_\ell$ 
9:   end for
10:  return  $\mathcal{T}_L$ 
11: end procedure

```

Algorithm 4 OED using the DIRT-based SAAs $\hat{\Psi}_X^N \approx \Psi_X := \mathbb{E}_{\pi_{\mathbf{d}|\mathbf{e}}}[\psi_X(\mathbf{e}, \mathbf{d})]$.

```

1: procedure OED( $\rho_{\mathbf{e}, \mathbf{d}, \mathbf{m}}, p_{\mathbf{e}, \mathbf{d}, \mathbf{m}}, \pi_{\mathbf{m}}, X, N$ )                                #  $p_{\mathbf{e}, \mathbf{d}, \mathbf{m}}$ : unnormalized joint density
2:    $\mathcal{T} \leftarrow$  DIRT( $\rho_{\mathbf{e}, \mathbf{d}, \mathbf{m}}, p_{\mathbf{e}, \mathbf{d}, \mathbf{m}}$ )
3:   if  $X = D$  then                                                                    # D-optimal designs
4:     Choose  $\mathbf{e}^* \in \text{Arg max}_{\mathbf{e} \in \mathcal{E}} \text{DOpt}(\rho_{\mathbf{e}, \mathbf{d}, \mathbf{m}}, \mathcal{T}, \pi_{\mathbf{m}}, \mathbf{e}, N)$            # Using Algorithm 2
5:   end if
6:   if  $X = A$  then                                                                    # A-optimal designs
7:     Choose number of inner samples  $M$ 
8:     Choose  $\mathbf{e}^* \in \text{Arg max}_{\mathbf{e} \in \mathcal{E}} \text{AOpt}(\rho_{\mathbf{e}, \mathbf{d}, \mathbf{m}}, \mathcal{T}, \mathbf{e}, N, M)$            # Using Algorithm 1
9:   end if
10:  return  $\mathbf{e}^*$ 
11: end procedure

```

Remark 4.3. While (4.13) shows that the approximation error of the composite map can be controlled in the last layer, independent of the choice of bridging densities, (4.12) suggests that the choice of bridging densities plays a crucial role in the efficiency of the DIRT algorithm, since it influences the maximal ranks required for approximating $\sqrt{(\mathcal{T}_{\ell-1})^\# p_{\mathbf{e}, \mathbf{d}, \mathbf{m}}^\ell}$ in each layer. The bridging densities can be defined in various ways and what constitutes a smart choice is problem-dependent. One generally suitable option

is the tempering approach [29]. Given a sequence of temperatures $0 = \beta_0 < \beta_1 < \dots < \beta_L = 1$, the ℓ -th tempered bridging density can be defined as $\pi_{\mathbf{e}, \mathbf{d}, \mathbf{m}}^\ell = \left(\frac{\pi_{\mathbf{e}, \mathbf{d}, \mathbf{m}}}{\rho_{\mathbf{e}, \mathbf{d}, \mathbf{m}}} \right)^{\beta_\ell} \rho_{\mathbf{e}, \mathbf{d}, \mathbf{m}}$ or $\pi_{\mathbf{e}, \mathbf{d}, \mathbf{m}}^\ell = (\pi_{\mathbf{e}, \mathbf{d}, \mathbf{m}})^{\beta_\ell}$. Alternatively, in the case of Bayesian inference, if one is interested in approximating a highly concentrated posterior density stemming from an inverse problem with a large amount of data, it may be beneficial to build the bridging densities by adding the data sequentially in batches as ℓ increases.

We conclude this section with some comments regarding the assumptions required in the proof of the error estimate in Theorem 3.7. The first key assumption, $\mathcal{D}_H(\hat{\pi}_{\mathbf{e}, \mathbf{d}, \mathbf{m}}, \pi_{\mathbf{e}, \mathbf{d}, \mathbf{m}}) \leq \varepsilon$ for some $\varepsilon \in (0, 1]$, can be guaranteed by building a sufficiently accurate FTT decomposition in the last layer of the DIRT procedure. Secondly, the assumption of an upper bound on the ratio of the posterior density $\pi_{\mathbf{m}|\mathbf{e}, \mathbf{d}}$ and its DIRT-based approximation $\hat{\pi}_{\mathbf{m}|\mathbf{e}, \mathbf{d}}$ is guaranteed by employing the defensive approximation to the target density (4.8).

The more stringent and questionable assumption is (3.25). Since $\hat{\pi}_{\mathbf{m}|\mathbf{e}, \mathbf{d}} > 0$ by design, if $\pi_{\mathbf{m}}(\mathbf{m}) = 0$ for some $\mathbf{m} \in \mathcal{M}$, the assumption is clearly violated. In practice, however, our integration domain is restricted to some bounded box that is strictly contained in the support of the prior density $\pi_{\mathbf{m}}$. Thus, as long as the box and prior are chosen such that $\pi_{\mathbf{m}}$ is bounded away from zero in the restricted domain, the assumption holds, at least for Gaussian or uniform priors. However, the bound $c_2(\mathbf{e})$ from (3.25) can get arbitrarily large as the number of experiments increases.

In practice, we find the approximation errors to be reasonable (and proportional to $\mathcal{D}_H(\pi_{\mathbf{e}, \mathbf{d}, \mathbf{m}}, \hat{\pi}_{\mathbf{e}, \mathbf{d}, \mathbf{m}})$) when the dimensions of \mathbf{e} and \mathbf{d} are not large, e.g., when choosing a small number of experiments to perform in a batch-OED setting or a sequential OED setting, outlined in the next section.

5. SEQUENTIAL OPTIMAL EXPERIMENTAL DESIGN USING CONDITIONAL DIRT

For certain applications, e.g. medical imaging or weather prediction, data is accumulated in a sequential fashion. With each incoming data set, the posterior distribution is updated to account for the knowledge gained from the new observations. These settings lend themselves naturally to *adaptive* or *sequential* optimal design (SOED). In SOED, experimental conditions or designs are chosen in stages to optimize an *incremental* utility function that incorporates the current state of knowledge (i.e., posterior) about the unknown parameters. In Section 5.1, we describe a greedy approach to solving the SOED problem and identify the main challenges in finding such optimal sequential designs. The transport map approach for OED described in Section 3.3 is extended to sequential OED in Section 5.2. Expanding on Section 4, we then discuss how to construct preconditioners for efficient FTT-based approximations to the SOED objective functions in Section 5.3.

5.1. A greedy approach to sequential optimal experimental design. While the OED formulation described in the preceding sections focuses on finding designs given only prior information, in SOED the posterior is iteratively updated and designs are chosen adaptively in distinct stages. As for OED, optimality is defined in terms of the level of uncertainty in the posterior distribution. However, the key difference between OED and SOED is the inclusion of a feedback loop into the optimization problem, as visualized in Figure 5.1.

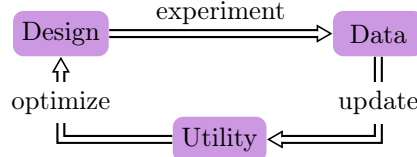


FIGURE 5.1. Flowchart for an SOED procedure depicting the feedback loop between finding optimal designs, using them to conduct the experiment and collect data, and updating the state of knowledge and utility function using the newly-collected data.

For a fixed budget of $K \in \mathbb{N}$ experiments, the solution to the SOED problem is a set of design functions (or policies) $\{e_k^*(\pi_{\mathbf{m}}^{k-1})\}_{k=1}^K$ that depend on the current state of knowledge about \mathbf{m} , which is

defined by the posterior density $\{\pi_{\mathbf{m}}^k\}_{k=0}^{K-1}$. Finding the optimal set of design functions requires solving a dynamic programming problem as described in [35, Chapter 3]. However, the numerical solution of such a dynamic programming problem is extremely costly, since it involves nested optimization and thus suffers from the curse of dimensionality.

Thus, we employ a greedy approach to solving the SOED problem. Unlike the dynamic programming formulation, the greedy formulation of SOED is myopic. Rather than computing all K optimal policies *simultaneously*, future optimal experimental conditions are chosen in small batches given the current state of knowledge, hence the curse of dimensionality is avoided. Due to this simplification, the sequential designs $\{\mathbf{e}_k^*\}_{k=1}^K$ obtained using the greedy optimization approach will generally be *sub-optimal* for a fixed number of experiments K . However, the approach does have advantages in the absence of a hard limit on the number of experiments that can be performed. Additional experiments can be included seamlessly using the greedy approach, whereas the number of experiments must be chosen a priori in the dynamic programming context.

To facilitate the discussion, we define a recursive formula for updating the state of knowledge, or posterior density, between experimental stages:

$$(5.1) \quad \pi_{\mathbf{m}}^k := \pi_{\mathbf{m}|e_k, \mathbf{d}_k, \mathbf{I}_{k-1}} = \frac{\pi_{\mathbf{d}_k|\mathbf{m}, e_k, \mathbf{I}_{k-1}} \cdot \pi_{\mathbf{m}}^{k-1}}{\pi_{\mathbf{d}_k|e_k, \mathbf{I}_{k-1}}} = \frac{\pi_{\mathbf{d}_k|\mathbf{m}, e_k, \mathbf{I}_{k-1}} \cdot \pi_{\mathbf{m}|\mathbf{I}_{k-1}}}{\pi_{\mathbf{d}_k|e_k, \mathbf{I}_{k-1}}},$$

for $k = 1, \dots, K$, where $\mathbf{I}_{k-1} := \{(\mathbf{e}_i^*, \mathbf{d}_i^*)\}_{i=1}^{k-1}$ stores the history of optimal designs and their corresponding observations up until stage $k-1$. We define $\pi_{\mathbf{m}}^0 := \pi_{\mathbf{m}}$ to be the prior, and \mathbf{I}_0 to be the empty set, $\mathbf{I}_0 := \emptyset$. In deriving the last equality, we have assumed that the stage $k-1$ posterior is independent of the decision to be made at the next stage, i.e., $\pi_{\mathbf{m}|e_k, \mathbf{I}_{k-1}} = \pi_{\mathbf{m}|\mathbf{I}_{k-1}}$.

In the greedy approach to SOED, given the current state of knowledge, the k -th design vector \mathbf{e}_k^* is chosen to optimize the stage k reward,

$$(5.2) \quad \Psi^k(e_k, \pi_{\mathbf{m}}^{k-1}) = \mathbb{E}_{\pi_{\mathbf{d}_k|e_k, \mathbf{I}_{k-1}}} [\psi^k(e_k, \mathbf{d}_k, \pi_{\mathbf{m}}^{k-1})],$$

which is an expectation of a stage k utility function ψ^k . As before, the SOED utility function is problem-specific and there are analogies to the A- and D-optimality criteria defined for OED in (2.5) and (2.6).

For the remainder of this section, we focus on the D-optimal SOED utility function, ψ_D^k , which for $k = 1, \dots, K$ is defined as

$$(5.3) \quad \psi_D^k(e_k, \mathbf{d}_k, \pi_{\mathbf{m}}^{k-1}) = \mathcal{D}_{\text{KL}}(\pi_{\mathbf{m}|e_k, \mathbf{d}_k, \mathbf{I}_{k-1}} \| \pi_{\mathbf{m}}^{k-1}) = \mathcal{D}_{\text{KL}}(\pi_{\mathbf{m}|e_k, \mathbf{d}_k, \mathbf{I}_{k-1}} \| \pi_{\mathbf{m}|\mathbf{I}_{k-1}}).$$

The D-optimal, greedy sequential designs are obtained by maximizing the *incremental* expected information gain in each stage of the procedure. For generality, we allow the design and observation spaces to vary between stages and denote the stage-dependent spaces by \mathcal{E}_k and \mathcal{D}_k respectively. The general approach for finding greedy sequential designs using the EIG criterion is summarized as follows:

- (1) Initialize $\pi_{\mathbf{m}}^0 = \pi_{\mathbf{m}}$, $\mathbf{I}_0 = \emptyset$, and $k = 1$.
- (2) At stage k , find an optimal k -th design vector \mathbf{e}_k^* that maximizes

$$\Psi_D^k(e_k, \pi_{\mathbf{m}}^{k-1}) = \mathbb{E}_{\pi_{\mathbf{d}_k|e_k, \mathbf{I}_{k-1}}} [\psi_D^k(e_k, \mathbf{d}_k, \pi_{\mathbf{m}}^{k-1})]$$

over $e_k \in \mathcal{E}_k$.

- (3) Perform experiment k with design vector \mathbf{e}_k^* to obtain data $\mathbf{d}_k^* \in \mathcal{D}$.
- (4) Update $\mathbf{I}_k = \{\mathbf{I}_{k-1}, \mathbf{e}_k^*, \mathbf{d}_k^*\}$ and $\pi_{\mathbf{m}}^k = \pi_{\mathbf{m}|\mathbf{I}_k}$.
- (5) Increment k and repeat [steps \(2\) to \(4\)](#) until all experiments have been performed or sufficient reduction in posterior uncertainty has been achieved.

In the following section we focus on [step \(2\)](#) and extend the KR-based approach of [Section 3](#) to numerically approximate the incremental expected information gain Ψ_D^k .

5.2. Knothe-Rosenblatt-based approximation to sequential D-optimal BOED. Assume we have access to a KR map \mathcal{T}^k coupling a reference density $\rho_{e, \mathbf{d}, \mathbf{m}}$ to the k -th joint conditional density, which in the most general form satisfies

$$(5.4) \quad \pi_{e_k, \mathbf{d}_k, \mathbf{m}|\mathbf{I}_{k-1}} = \pi_{\mathbf{d}_k|e_k, \mathbf{m}, \mathbf{I}_{k-1}} \cdot \pi_{\mathbf{m}|\mathbf{I}_{k-1}} \cdot \pi_{e_k|\mathbf{I}_{k-1}} = \pi_{\mathbf{d}_k|e_k, \mathbf{m}, \mathbf{I}_{k-1}} \cdot \pi_{\mathbf{m}}^{k-1} \cdot \pi_{e_k|\mathbf{I}_{k-1}}.$$

The k -th incremental likelihood $\pi_{\mathbf{d}_k|\mathbf{e}_k, \mathbf{m}, \mathbf{I}_{k-1}}$ and the design density $\pi_{\mathbf{e}_k|\mathbf{I}_{k-1}}$ are both specified via the model (see Remark 5.1). Then the stage k incremental expected information gain,

$$\Psi_D^k(\mathbf{e}_k, \pi_{\mathbf{m}}^{k-1}) = \mathbb{E}_{\pi_{\mathbf{d}_k|\mathbf{e}_k, \mathbf{I}_{k-1}}} [\psi_D^k(\mathbf{e}_k, \mathbf{d}_k, \pi_{\mathbf{m}}^{k-1})],$$

can be approximated at any $\mathbf{e}_k \in \mathcal{E}_k$ using Algorithm 2,

$$(5.5) \quad \Psi_D^k(\mathbf{e}_k, \pi_{\mathbf{m}}^{k-1}) \approx \hat{\Psi}_D^k(\mathbf{e}_k, \pi_{\mathbf{m}}^{k-1}) := \text{DOPT}(\rho_{\mathbf{e}, \mathbf{d}, \mathbf{m}}, \mathcal{T}^k, \pi_{\mathbf{m}}^{k-1}, \mathbf{e}_k, N).$$

While this approach is straightforward, it suffers from a few drawbacks. The first major issue is that we generally do not have a closed-form expression for the posterior $\pi_{\mathbf{m}}^{k-1}$, hence we cannot execute step 6 of Algorithm 2, which requires evaluation of the density $\pi_{\mathbf{m}}^{k-1}$ at the sample parameters. The second major issue is a computational one. While we could employ Algorithm 3 to construct an approximate map \mathcal{T}^k at each stage, the target density $\pi_{\mathbf{e}_k, \mathbf{d}_k, \mathbf{m}|\mathbf{I}_{k-1}}$ gets progressively more concentrated as data is collected. Thus, constructing the KR rearrangement using DIRT gets successively more costly in terms of the number of unnormalized density evaluations and FLOPs, as k increases. A sufficiently accurate approximation also requires an increasing number of layers in DIRT. Additionally, the posteriors tend to concentrate sequentially to some subdomain as data is collected and we should exploit this structure to avoid wasting computational resources. All those challenges are addressed in Section 5.3.

Remark 5.1 (Incremental likelihood and density). *The exact forms of the incremental likelihood $\pi_{\mathbf{d}_k|\mathbf{e}_k, \mathbf{m}, \mathbf{I}_{k-1}}$ and the k -th design density $\pi_{\mathbf{e}_k|\mathbf{I}_{k-1}}$ are model-dependent. For example, if one couples the k -th observations $\mathbf{d}_k \in \mathcal{D}_k$, k -th designs $\mathbf{e}_k \in \mathcal{E}_k$, and the inference parameters \mathbf{m} via*

$$(5.6) \quad \mathbf{d}_k = \mathcal{F}(\mathbf{e}_k, \mathbf{m}) + \boldsymbol{\eta}_k, \quad \boldsymbol{\eta}_k \sim \mathcal{N}(0, \sigma_k^2 \text{id}),$$

and assumes the only explicit dependence on the history vector \mathbf{I}_{k-1} is through the prior $\mathbf{m} \sim \pi_{\mathbf{m}|\mathbf{I}_{k-1}}$ at stage k , then the stage- k likelihood is independent of \mathbf{I}_{k-1} and satisfies

$$(5.7) \quad \pi_{\mathbf{d}_k|\mathbf{e}_k, \mathbf{m}} \propto \exp\left[-\frac{1}{2\sigma_k^2} \|\mathcal{F}(\mathbf{e}_k, \mathbf{m}) - \mathbf{d}_k\|^2\right].$$

This is the form of the k -th likelihood used in Section 6. Likewise, the design density is independent of \mathbf{I}_{k-1} , i. e., $\pi_{\mathbf{e}_k|\mathbf{I}_{k-1}} = \pi_{\mathbf{e}_k}$.

5.3. Preconditioned Knothe-Rosenblatt maps for SOED. To alleviate the drawbacks of the straightforward approach, we propose a preconditioning method that enables incorporation of previously acquired knowledge. This approach helps reduce the number of layers required in the sequential construction of the DIRT maps $\{\mathcal{T}^k\}_{k=1}^K$ and in the amount of unnormalized density evaluations needed for constructing the FTT decomposition. The idea driving the preconditioning approach is similar to the reasoning behind the layered construction of deep inverse Rosenblatt transports in [20].

Assume we have access to a KR-based approximation of the posterior, $(\mathcal{T}_{\mathbf{m}}^k)_{\#} \rho_{\mathbf{m}} = \hat{\pi}_{\mathbf{m}}^k \approx \pi_{\mathbf{m}|\mathbf{I}_k} =: \pi_{\mathbf{m}}^k$ for $k = 1, \dots, K-1$. To start, we approximate the k -th joint conditional density in (5.4) using the corresponding transport map surrogate,

$$(5.8) \quad \pi_{\mathbf{e}_k, \mathbf{d}_k, \mathbf{m}|\mathbf{I}_{k-1}} \approx \pi_{\mathbf{d}_k|\mathbf{e}_k, \mathbf{m}, \mathbf{I}_{k-1}} \cdot \hat{\pi}_{\mathbf{m}|\mathbf{I}_{k-1}} \cdot \pi_{\mathbf{e}_k|\mathbf{I}_{k-1}} =: \tilde{\pi}_{\mathbf{e}_k, \mathbf{d}_k, \mathbf{m}|\mathbf{I}_{k-1}}.$$

Then, we construct a KR rearrangement to the pullback density, \mathcal{K}^k to $(\mathcal{L}^k)^{\#} \tilde{\pi}_{\mathbf{e}_k, \mathbf{d}_k, \mathbf{m}|\mathbf{I}_{k-1}}$, where \mathcal{L}^k is a stage k diagonal preconditioner of the form

$$(5.9) \quad \mathcal{L}^k(\mathbf{z}) := \mathcal{L}^k(\mathbf{z}_e, \mathbf{z}_d, \mathbf{z}_m) = \begin{bmatrix} \mathcal{R}_e^k(\mathbf{z}_e) \\ \text{id}_d(\mathbf{z}_d) \\ \mathcal{T}_m^k(\mathbf{z}_m) \end{bmatrix}$$

with $\mathbf{z}_e \in \mathbb{R}^{n_e}$, $\mathbf{z}_d \in \mathbb{R}^{n_d}$, $\mathbf{z}_m \in \mathbb{R}^{n_m}$ and \mathcal{R}_e^k denoting a KR rearrangement such that $(\mathcal{R}_e^k)_{\#} \rho_e = \pi_{\mathbf{e}_k|\mathbf{I}_{k-1}}$. If \mathcal{R}_e^k is not known, it could be replaced by the identity operator id_e . Using the preconditioner (5.9) such that $(\mathcal{L}^k)_{\#} \rho_{\mathbf{e}, \mathbf{d}, \mathbf{m}} \propto \pi_{\mathbf{e}_k} \rho_d \hat{\pi}_{\mathbf{m}|\mathbf{I}_{k-1}}$, the k -th preconditioned density $(\mathcal{L}^k)^{\#} \tilde{\pi}_{\mathbf{e}_k, \mathbf{d}_k, \mathbf{m}|\mathbf{I}_{k-1}}$, which we aim to approximate, is

$$(\mathcal{L}^k)^{\#} \tilde{\pi}_{\mathbf{e}_k, \mathbf{d}_k, \mathbf{m}|\mathbf{I}_{k-1}} \propto \pi_{\mathbf{d}_k|\mathbf{e}_k, \mathbf{m}, \mathbf{I}_{k-1}}(\mathbf{z}_d | \mathcal{R}_e^k(\mathbf{z}_e), \mathcal{T}_m^k(\mathbf{z}_m)) \rho_e(\mathbf{z}_e) \rho_{\mathbf{m}}(\mathbf{z}_m).$$

The KR map \mathcal{K}^k is built using [Algorithm 3](#), such that $(\mathcal{K}^k)_\# \rho_{e,d,m} \approx (\mathcal{L}^k)_\# \tilde{\pi}_{e_k,d_k,m|I_{k-1}}$. This requires significantly fewer density evaluations in practice than constructing a KR rearrangement to $\pi_{e_k,d_k,m|I_{k-1}}$. Once \mathcal{K}^k is constructed, the composite map $\mathcal{T}^k = \mathcal{L}^k \circ \mathcal{K}^k$ provides a coupling between the reference $\rho_{e,d,m}$ and the k -th approximation to the joint target $\tilde{\pi}_{e_k,d_k,m|I_{k-1}}$.

The maps \mathcal{T}_m^k required for defining the preconditioner are constructed in a recursive fashion using a running approximation to the posterior density $\pi_{m|I_{k-1}}$. Assuming $(\mathcal{T}_m^{k-1})_\# \rho_m \approx \pi_{m|I_{k-1}}$, $\mathcal{T}_m^k := \mathcal{T}_m^{k-1} \circ \mathcal{K}_m^k$, where \mathcal{K}_m^k is a KR map satisfying $(\mathcal{K}_m^k)_\# \rho_m = (\mathcal{T}_m^{k-1})_\# \pi_{m|I_k}$. This could be viewed as employing a DIRT-based construction to the stage $K-1$ posterior $\pi_{m|I_{K-1}}$ guided by the bridging densities $\{\pi_{m|I_k}\}_{k=1}^{K-1}$. As mentioned in [Remark 4.3](#), these bridging densities are a natural choice for posteriors stemming from Bayesian inverse problems with large amounts of data, or for sequential Bayesian inference.

Remark 5.2 (DIRT map approximation to the posterior densities). *Since the sequence of posterior densities $\{\pi_{m|I_k}\}_{k=1}^{K-1}$ are obtained by performing experiments with conditions that maximize the incremental expected information gain $\mathcal{D}_{\text{KL}}(\pi_{m|e_{k+1},d_{k+1},I_k} \| \pi_{m|I_k})$, the distance between adjacent posteriors may be quite large. Thus, the ranks required to approximate the square root of $(\mathcal{T}_m^{k-1})_\# \pi_{m|I_k}$ in one step may be large. For certain problems it is more efficient to combine the tempering approach discussed in [Section 4.3](#) with the sequential data accumulation approach discussed in [Section 5.3](#) to obtain a composite set of bridging densities.*

Due to the recursive layered approximation to the posterior density, there is a sequential accumulation of error in the KR approximation to $\pi_{e_k,d_k,m|I_{k-1}}$. However, this error can be controlled using [Lemma 4.1](#). The amount of additional applications of the PTO map required to keep the running approximation to the posterior density is generally offset by the reduction in computational work due to using the resulting preconditioning operator \mathcal{L}^k defined in (5.9). We present the full posterior-preconditioned SOED procedure in [Algorithm 5](#), where we again leave the optimization algorithm for maximizing the incremental EIG arbitrary. A visual representation of the algorithm in the form of a flowchart is also included in [Figure 5.2](#).

Algorithm 5 Greedy posterior-preconditioned SOED algorithm using the incremental EIG criterion.

```

1: procedure SOED( $K, \rho_{e,d,m}, \pi_{e_1}, \pi_m, \pi_{d_1|e_1,m}$ )
2:    $\mathcal{L}^0 \leftarrow \text{id}_n, \mathcal{T}_m^0 \leftarrow \text{id}_{n_m}, \hat{\pi}_m^0 \leftarrow \pi_m, \mathbf{I}_0 = \emptyset$  # Initialization
3:   for  $k = 1, \dots, K$  do
4:      $\pi_{e_k,d_k,m|I_{k-1}} \leftarrow \pi_{d_k|e_k,m,I_{k-1}} \cdot \hat{\pi}_m^{k-1} \cdot \pi_{e_k|I_{k-1}}$ 
5:      $\mathcal{K}^k \leftarrow \text{DIRT}(\rho_{e,d,m}, (\mathcal{L}^k)_\# \pi_{e_k,d_k,m|I_{k-1}})$  # Using Algorithm 3
6:      $\mathcal{T}^k \leftarrow \mathcal{L}^k \circ \mathcal{K}^k$ 
7:     Choose  $e_k^* \in \text{Arg max}_{e_k \in \mathcal{E}} \text{DOpt}(\rho_{e,d,m}, \mathcal{T}^k, \hat{\pi}_m^{k-1}, e_k)$  # Using Algorithm 2
8:     Perform experiment with  $e_k^*$  and acquire  $d_k^*$ 
9:     Update  $\mathbf{I}_k = \{\mathbf{I}_{k-1}, e_k^*, d_k^*\}$ 
10:     $\mathcal{K}_m^k \leftarrow \text{DIRT}(\rho_m, (\mathcal{T}_m^{k-1})_\# \pi_{m|I_k})$  # Using Algorithm 3
11:     $\mathcal{T}_m^k = \mathcal{T}_m^{k-1} \circ \mathcal{K}_m^k, \hat{\pi}_m^k \leftarrow (\mathcal{T}_m^k)_\# \rho_m$ 
12:    Update  $\mathcal{L}^k$  using equation (5.9) and  $\mathcal{T}_m^k$ 
13:  end for
14:  return  $\{e_k^*\}_{k=0}^{K-1}, \{d_k^*\}_{k=0}^{K-1}, \mathcal{T}_m^{K-1}$ 
15: end procedure

```

6. NUMERICAL EXAMPLES

We demonstrate the effectiveness of our proposed method on finding optimal designs for two model problems. In [Section 6.1](#), we consider a non-intrusive sensor placement problem using transport-map-based procedures ([Algorithm 5](#) and [Algorithm 4](#)) to compute optimal testing times for an inverse problem in disease modeling. In [Section 6.2](#), we consider instead intrusive designs, i.e., we choose optimal

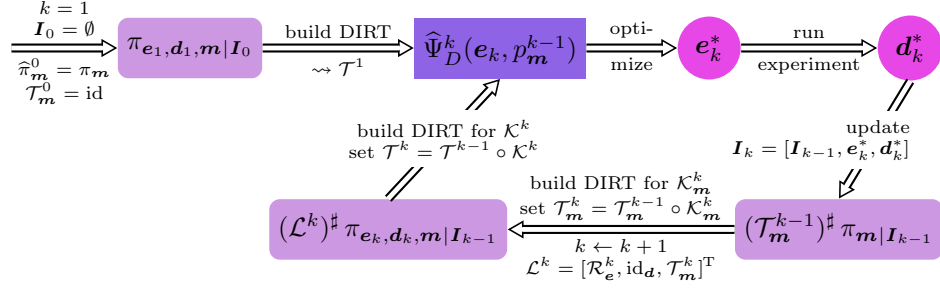


FIGURE 5.2. Flowchart visualization of the greedy preconditioned SOED procedure outlined in Algorithm 5.

boundary conditions for an inverse problem with an elliptic forward operator. The algorithms used in both examples are implemented in MATLAB using the DIRT FTT codes from the `deep-tensor toolbox` [19].

6.1. Optimal observation times for parameter inversion using the SEIR disease model. As a first example, we consider the susceptible-exposed-infected-removed (SEIR) model, commonly used for describing the spread of infectious diseases. Under the assumption of constant population size, the SEIR model is comprised of the following system of ordinary differential equations,

$$(6.1) \quad \begin{aligned} \frac{dS}{dt} &= -\beta(t) S I, & \frac{dE}{dt} &= \beta(t) S I - \alpha E, \\ \frac{dI}{dt} &= \alpha E - \gamma(t) I, & \frac{dR}{dt} &= (\gamma^r + \gamma^d(t)) I, \end{aligned}$$

where the variables $S(t), E(t), I(t), R(t)$ are used to denote the fractions of susceptible, exposed, infected and removed individuals at time t , respectively, and are initialized with $S(0) = 99$, $E(0) = 1$, and $I(0) = R(0) = 0$. The parameters to be estimated are $\beta(t), \alpha, \gamma^r, \gamma^d(t)$, where the constants α and γ^r denote the rate of susceptibility to exposure and infection to recovery, respectively. To simulate the effect of policy changes or other time-dependent factors (e. g., quarantine and overcrowding of hospitals), the rates at which exposed individuals become infected and infected individuals perish are assumed to be time-dependent and parametrized as follows:

$$\beta(t) = \beta_1 + \frac{\tanh(7(t - \tau))}{2}(\beta_2 - \beta_1), \quad \gamma^d(t) = \gamma_1^d + \frac{\tanh(7(t - \tau))}{2}(\gamma_2^d - \gamma_1^d),$$

i. e., the rates transition smoothly from some initial rate (β_1 and γ_1^d) to some final rate (β_2 and γ_2^d) around time $\tau > 0$.

In the following, we fix $\tau = 2.1$ and an overall time interval of $[0, 4]$. The time interval $[1, 3]$ is split into 4 disjoint subintervals, $\{(a_i, a_{i+1})\}_{i=1}^4$ (with $a_i = 1 + 0.5(i - 1)$) and the goal of the optimal design problem is to choose four times $e_i \in (a_i, a_{i+1})$, one in each interval, at which to measure the number of infected and deceased individuals for optimal inference of the 6 rates $\mathbf{m} = [\beta_1, \alpha, \gamma^r, \gamma_1^d, \beta_2, \gamma_2^d]$. We consider two ways to find the four optimal times e_1, \dots, e_4 : (i) choosing them one at a time using a greedy sequential procedure (yielding the optimal design vector $\mathbf{e}_{\text{SOED-1}}^*$), and (ii) planning two subsequent observation times simultaneously using a greedy sequential procedure (yielding the optimal design vector $\mathbf{e}_{\text{SOED-2}}^*$). To set up the Bayesian inverse problem, a uniform prior on $[0, 1]$ is assigned to each unknown rate, i. e., $\pi_{\mathbf{m}} = \mathbb{1}_{[0, 1]^6}$. The measurement noise at each observation time is assumed to be uncorrelated and Gaussian with zero mean and standard deviation $\sigma_I = 2$ for the measured number of infected individuals and $\sigma_{R^d} = 1$ for the measured number of deceased individuals.

We choose a fixed “true” parameter $\mathbf{m}_{\text{true}} = [0.4, 0.3, 0.3, 0.1, 0.15, 0.6]^T$ in the following experiments and focus on finding designs maximizing the EIG, i. e., the D-optimality criterion. For all experiments, the dynamics are simulated in MATLAB using `ode45` to solve the system of equations (6.1), while MATLAB’s `fmincon` function is used to maximize the objective function. Simple bound constraints ensure that

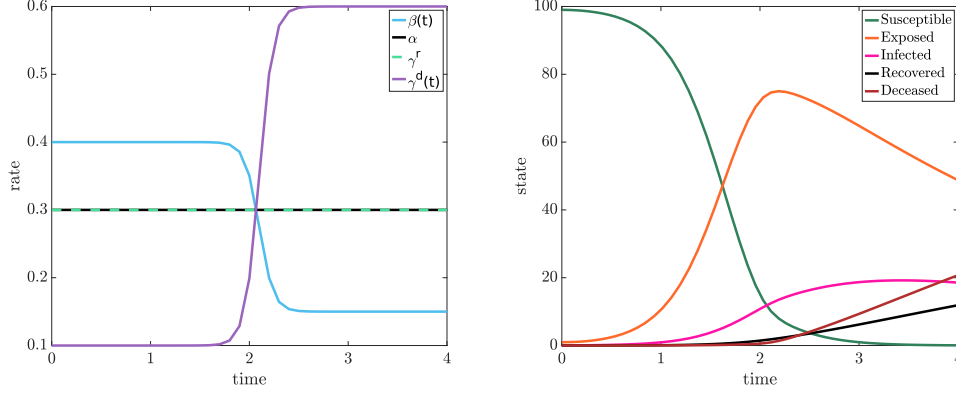


FIGURE 6.1. The true rates used for synthesizing data and the corresponding solution to the system (6.1) are visualized on the left and right, respectively.

e_i remains inside the corresponding time interval. A visualization of the true rates as well as the corresponding solution to the SEIR model (6.1) is provided in Figure 6.1

We begin with experiment (ii). Using Algorithm 4 with $N = 10\,000$ samples to approximate the EIG, we solve the greedy sequential design problem and plan the four optimal observation times two at a time, leading to the final optimal design vector $\mathbf{e}_{\text{SOED-2}}^*$. Construction of the DIRT approximation to the two joint densities for the $4 + 2 + 6 = 12$ -dimensional random variables $\mathbf{e}, \mathbf{d}, \mathbf{m}$ as well as the intermediate posterior density $\pi_{\mathbf{m}|\mathbf{e}_{1:2}^*, \mathbf{d}_{1:2}^*}$ required 350 650 evaluations of the corresponding unnormalized densities, and thus 350 650 solves of the SEIR ODE system, where each evaluation takes approximately 3.5×10^{-3} s on average.

We also find the optimal allocation of testing times in a purely sequential fashion ($\mathbf{e}_{\text{SOED-1}}^*$) for a fixed set of inference parameters using Algorithm 5, i.e., experiment (i). Again, $N = 10\,000$ samples are used to approximate the incremental EIG in each stage of the SOED procedure. The total procedure for finding four optimal observation times using the greedy sequential fashion required 147 987 solves of the SEIR ODE system.

Figure 6.2 provides a visual comparison of the posterior densities using data synthesized at the two “optimal” designs $\mathbf{e}_{\text{SOED-1}}^*$ and $\mathbf{e}_{\text{SOED-2}}^*$. They are also compared to the posterior density resulting from data measured uniformly at the beginning of each time interval, $\mathbf{e}_{\text{UNIF}} = [a_1, a_2, a_3, a_4]$. For each design choice, the resulting posterior density was estimated using the DIRT Algorithm 3 such that $\mathcal{D}_{\text{H}}(\hat{\pi}_{\mathbf{m}|\mathbf{e}^*, \mathbf{d}^*}, \pi_{\mathbf{m}|\mathbf{e}^*, \mathbf{d}^*})$ is around 10^{-2} . Both optimal design choices lead to more concentrated posterior densities than \mathbf{e}_{UNIF} over most of the parameters, however \mathbf{e}_{UNIF} outperforms both optimal designs in learning the infection rate α . The overall superiority of $\mathbf{e}_{\text{SOED-1}}^*$ and $\mathbf{e}_{\text{SOED-2}}^*$ is also supported by comparing the KL divergence from posterior to prior. Using 100 000 samples to approximate the KL divergence, we have:

$$\begin{aligned} \mathcal{D}_{\text{KL}}(\pi_{\mathbf{m}|\mathbf{e}_{\text{UNIF}}, \mathbf{d}_{\text{UNIF}}} \parallel \pi_{\mathbf{m}}) &\approx 5.1, \\ \mathcal{D}_{\text{KL}}(\pi_{\mathbf{m}|\mathbf{e}_{\text{SOED-1}}^*, \mathbf{d}_{\text{SOED-1}}} \parallel \pi_{\mathbf{m}}) &\approx 6.3, \\ \text{and } \mathcal{D}_{\text{KL}}(\pi_{\mathbf{m}|\mathbf{e}_{\text{SOED-2}}^*, \mathbf{d}_{\text{SOED-2}}} \parallel \pi_{\mathbf{m}}) &\approx 6.8. \end{aligned}$$

While the simultaneous planning of two experiments at a time in the greedy SOED procedure requires more solves of the SEIR system, it leads to a much better estimate of the initial rate of mortality (γ_1^d) and a slightly better estimate of the final rate of mortality (γ_2^d), in alignment with the larger value of the KL divergence.

Remark 6.1 (On the lack of information about the final rate of exposure β_2). *We note that all the designs struggle with learning the final rate of exposure β_2 , but this is a consequence of the transition time lying quite late in the simulation interval. Once the policies are implemented, almost all susceptible*

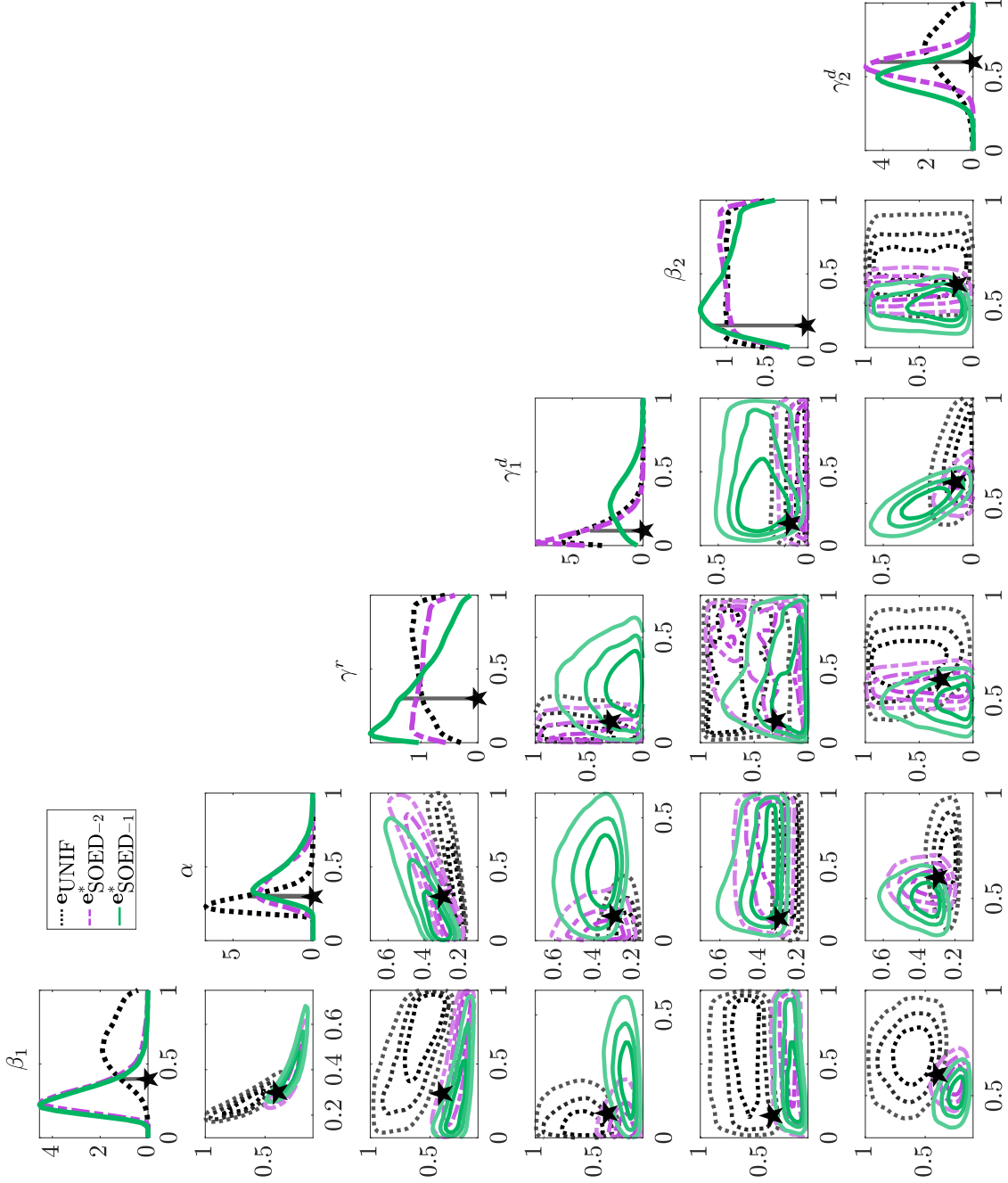


FIGURE 6.2. Visualization of the marginals of the posterior densities obtained using different observation times for the SEIR model problem in [Section 6.1](#). The posterior depicted using the black dotted line is obtained using the uniform observation times $\mathbf{e}_{\text{UNIF}} = [1, 1.5, 2.0, 2.5]$. The purple dashed line is used to visualize the posterior obtained using the two-at-a-time greedy sequential designs $\mathbf{e}_{\text{SOED}-2}^*$ and the solid green line corresponds to the posterior obtained using the one-at-a-time sequential optimal times $\mathbf{e}_{\text{SOED}-1}^*$. In all cases, the data was synthesized using $\mathbf{m}_{\text{true}} = [0.4, 0.3, 0.3, 0.1, 0.15, 0.6]^T$, visualized with a black star and perturbed by noise.

individuals are already exposed, hence the difficulty. We have also performed this experiment with a smaller value of τ , in which case β_2 is more accurately estimated at the expense of the precision of some of the initial rates, e. g., the initial mortality rate γ_d .

In Figure 6.3, we compare the performance of the optimal designs, randomly chosen designs, and e_{UNIF} . For this comparison, we extended the observation times to include two additional intervals. The optimal observation times outperform the as-soon-as-possible uniform observation times and the randomly chosen designs, and the gap greatly increases after the first experiment, since our observation times can be better geared to \mathbf{m}_{true} due to the feedback loop. It slowly tapers off after four experiments once information begins to saturate. Interestingly, e_{UNIF} starts off as the worst design choice but after 6 experiments performs almost as well as the one-at-a-time greedy sequential design $e_{\text{SOED-1}}^*$.

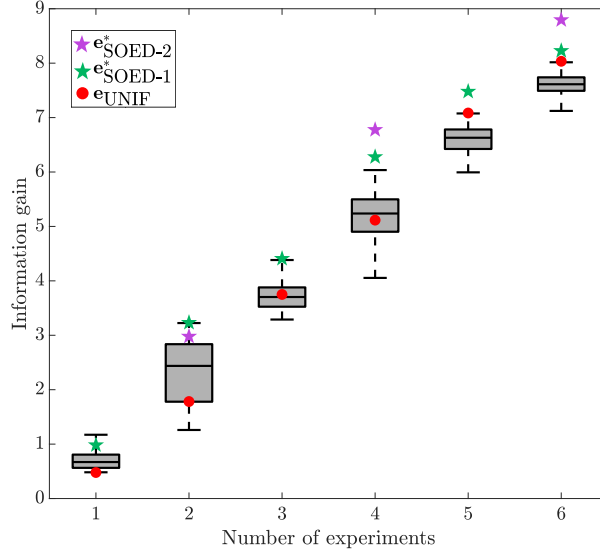


FIGURE 6.3. Boxplot comparing the effectiveness of the optimal observation times obtained for the SEIR example defined in Section 6.1 using the two-at-a-time and one-at-a-time procedures described in Section 6.1 (visualized using purple and green stars, resp.), randomly chosen observation times (visualized in black), and the uniform design e_{UNIF} (red circles). To obtain the results, data was synthesized using \mathbf{m}_{true} for the optimal designs ($e_{\text{SOED-1}}^*$ and $e_{\text{SOED-2}}^*$) and for 100 randomly chosen observation times. For each set of data and design, the information gain or $\mathcal{D}_{\text{KL}}(\pi_{\mathbf{m}|e,d} \parallel \pi_{\mathbf{m}})$ was approximated using 100 000 samples from a DIRT approximation to the posterior density $\pi_{\mathbf{m}|e,d}$.

6.2. Optimal Dirichlet data for permeability field inversion. Here, we consider the elliptic PDE

$$(6.2) \quad -\operatorname{div}(\kappa \nabla u) = 0 \quad \text{on } \Omega = (0, 1)^2,$$

which is often used in groundwater modeling. In this example, the inverse problem consists of estimating the spatially-dependent diffusivity field κ , given measurements of the pressure u at some pre-determined locations $(x_i, y_i) \in \Omega$. To ensure κ is nonnegative, we impose a Gaussian prior on the log diffusivity, $m = \log(\kappa) \sim \mathcal{N}(0, \mathcal{C}_{\text{pr}})$, with covariance operator \mathcal{C}_{pr} defined using a squared-exponential kernel

$$c(x, z) = \sigma_v^2 \exp \left[\frac{-\|x - z\|^2}{2 \ell^2} \right] \quad \text{for } x, z \in \Omega,$$

with $\sigma_v = 1$ and $\ell^2 = 0.1$. Employing a truncated Karhunen-Loève expansion of the unknown diffusivity field yields the approximation

$$m(x, \mathbf{m}) \approx \sum_{i=1}^{n_m} m_i \sqrt{\lambda_i} \phi_i(x),$$

where λ_i and $\phi_i(x)$ denote the i -th largest eigenvalue and eigenfunction of \mathcal{C}_{pr} , respectively, and the unknown coefficients $m_i \sim \mathcal{N}(0, 1)$. The Karhunen-Loève expansion is truncated after $n_m = 16$ modes, resulting in an approximation that captures 99 percent of the weight of \mathcal{C}_{pr} .

In this example, we consider an intrusive design, i. e., we choose Dirichlet data to impose at the left and right boundary, which we parametrize as

$$(6.3a) \quad u(x = 0, y) = \exp\left(-\frac{1}{2\sigma_w} (y - e_1)^2\right),$$

$$(6.3b) \quad u(x = 1, y) = -\exp\left(-\frac{1}{2\sigma_w} (y - e_2)^2\right).$$

Homogeneous Neumann data is fixed at the top and bottom boundaries. Thus, the design $\mathbf{e} = [e_1, e_2]$ enters into the parameter-to-state map directly through the boundary condition. The effect of different designs on the state can be seen in Figure 6.4. After each experiment is performed with some prescribed boundary conditions, u is measured at three locations as visualized in Figure 6.5.

Using Algorithm 5, boundary conditions are chosen for five experiments in a sequential fashion. The log-diffusivity field used to synthesize the data in each experiment is visualized in Figure 6.5. At each stage, the data is synthesized using the Fast Forward and Inverse problems solver (**FastFins**) package [18]. Specifically, the governing PDE (6.2) is solved using the finite element (FE) method with second-order Lagrange elements on a mesh of size $h = \frac{1}{64}$ in each coordinate direction. Applying the resulting discretized PTO map takes approximately 0.17 s. To speed up the construction of the FTT approximation to the joint density $\pi_{\mathbf{e}, \mathbf{d}, \mathbf{m} | \mathbf{I}_k}$ in each stage, the design-dependent parameter-to-state map is replaced with a surrogate built using the discrete empirical interpolation method [17]. The surrogate is constructed using the **FastFins** package with 1000 solves of the full-order elliptic PDE, and has relative approximation error on the order of 10^{-3} . One solve with the reduced-order model is approximately 60 times faster than one solve of the FE model.

As in the disease modeling example outlined in the previous section, in each stage of the SOED procedure, the bridging densities are obtained by tempering the likelihood. For this example, we construct a sequence of greedy optimal designs using both A- and D-optimality criteria. In the case of D-optimality, $N = 1000$ samples are used to approximate the expected information gain. To approximate the A-optimal sequential designs, $N = 500$ Quasi-Monte Carlo samples are used for the outer expectation with respect to the evidence, and $M = 1000$ Monte Carlo samples are used for the inner expectation. Table 6.1 presents the computational cost (given in terms of FE solves) for constructing DIRT approximations to the joint density $\pi_{\mathbf{e}_k, \mathbf{d}_k, \mathbf{m} | \mathbf{I}_{k-1}}$ and to the posterior $\pi_{\mathbf{m} | \mathbf{I}_k}$ in each SOED stage, $k = 1, \dots, 5$, as well as the cost for evaluating $\hat{\Psi}_A^N(\mathbf{e}_k)$ and $\hat{\Psi}_D^N(\mathbf{e}_k)$ once for any choice of design $\mathbf{e}_k \in \mathcal{E}_k$ in the optimization routine. For this particular problem, the A-optimal utility function exhibits smaller variations for different designs than the D-optimal one, so higher accuracy in the FTT surrogates to the joint densities are required (particularly in the later stages) to capture the correct “valleys” and “peaks”.

Figure 6.5 compares the means and the pointwise variances of the posterior distribution $\pi_{\mathbf{m} | \mathbf{e}_{1:5}, \mathbf{d}_{1:5}}$ using synthesized data from five experiments conducted with boundary conditions chosen randomly (i), as well as using the SOED procedure with both utility functions, ψ_A^k (ii) and ψ_D^k (iii). As made evident by both visualizations, the optimal designs perform much better at recovering the diffusivity channel. This observation is further strengthened in Figure 6.6, where both optimality criteria, ψ_A^k and ψ_D^k , are evaluated at the A- and D-optimal sequence of boundary conditions as well as at randomly chosen boundary conditions with data synthesized using the true log-diffusivity field.

While other methods like the nested Monte Carlo approach (e. g., see [37]) may need fewer samples in batch OED settings, they are generally not applicable to SOED without significant modifications. In contrast, our transport map approach adapts well to sequential settings. As shown in Table 6.1, computational costs tend to decrease across experimental stages due to the preconditioning approach

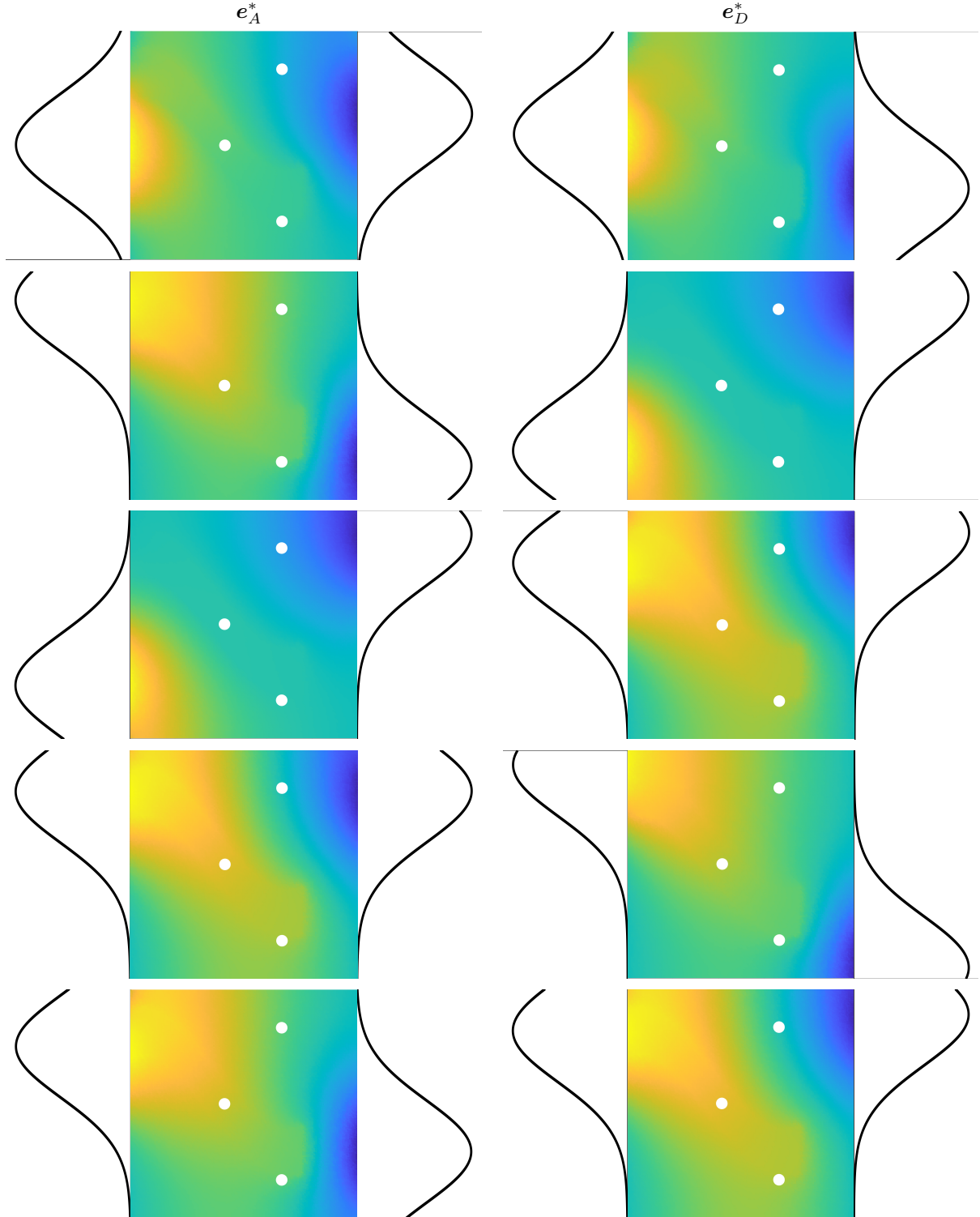


FIGURE 6.4. Visualization of optimal boundary conditions chosen using the greedy sequential procedure with the A-optimality criterion (left column) and D-optimality criterion (right column). The boundary conditions are plotted on the left and right boundaries in each figure and the corresponding state u is visualized for the true log diffusivity field.

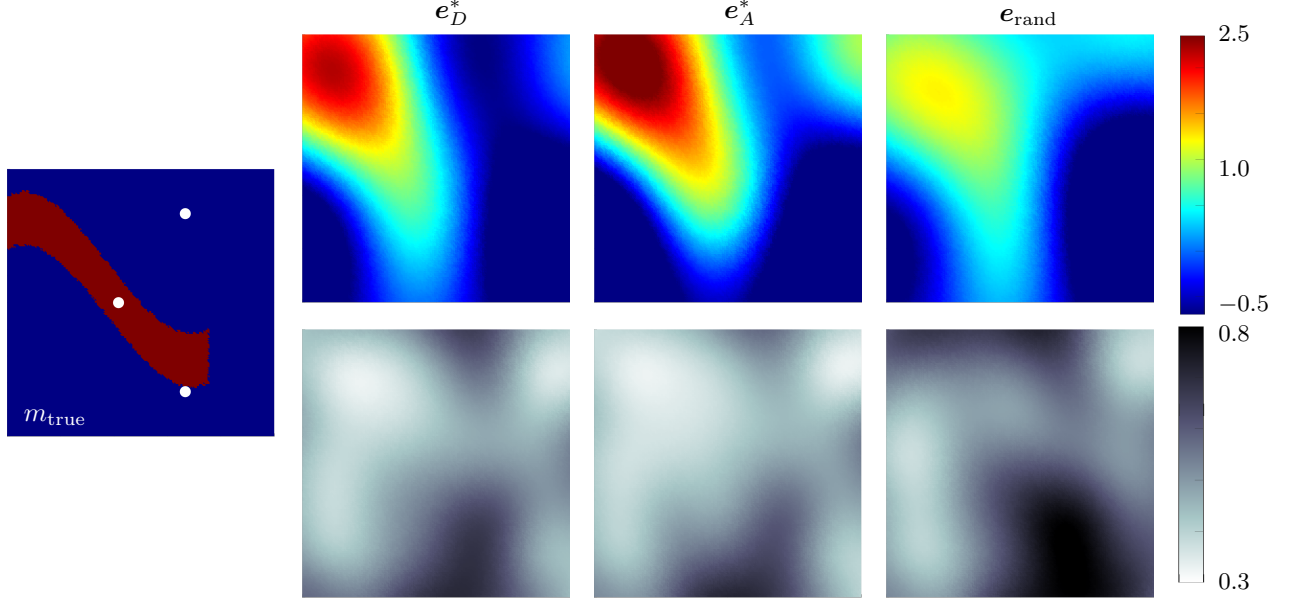


FIGURE 6.5. On the far left, the true log-diffusivity field used for synthesizing the pressure data at the three locations (visualized as white dots) is given. The top row in the 2×3 array of images visualizes the posterior mean obtained using five experiments with boundary conditions chosen using the greedy SOED procedure with the D-optimality criterion (e_D^*) and A-optimality criterion (e_A^*), and a randomly chosen design (e_{rand}). The bottom row visualizes the corresponding posterior pointwise variance for each design choice. The posterior means and variances were approximated using 100 000 samples from the corresponding approximate posterior density.

	Stage (k)	A-optimal	D-optimal
$\pi_{e_k, d_k, m I_{k-1}}$	1	4568	4339
	2	5850	4403
	3	5403	3058
	4	4568	1747
	5	3945	1898
$\hat{\Psi}_X^k(e_k)$	1	139	25
	2	87	24
	3	116	41
	4	139	50
	5	156	59
$\pi_{m I_k}$	1	632	595
	2	409	518
	3	494	419
	4	632	258
	5	428	309

TABLE 6.1. Computational cost, presented in terms of the number of FE solves of the underlying PDE, for constructing the DIRT approximations to $\pi_{e_k, d_k, m | I_{k-1}}$ and $\pi_{m | I_k^*}$, as well as the evaluation of the incremental optimality criterion $\hat{\Psi}_X^k$, in each SOED stage k . Note that the A-optimality criterion $\hat{\Psi}_A^k$ was evaluated in parallel using 50 workers, whereas the D-optimality criterion was evaluated in serial. However, the D-optimality criterion could also be easily parallelized.

described in Section 5.3. Moreover, after conducting experiments, the KR rearrangement provides an approximation to the posterior that can either be used directly or to enhance MCMC sampling efficiency.

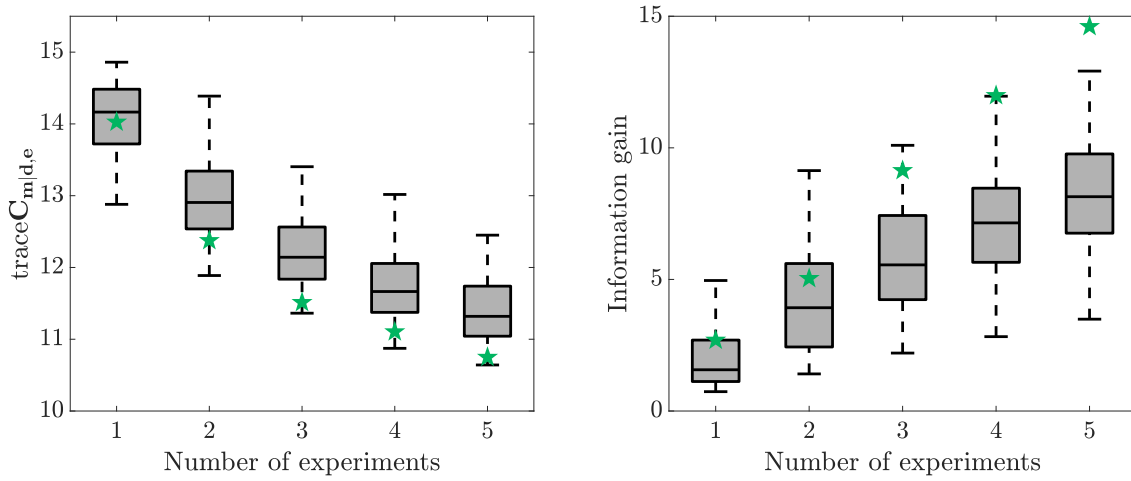


FIGURE 6.6. On the left, $\text{trace}(\mathbf{C}_{m|I_k})$, and on the right, $\mathcal{D}_{\text{KL}}(\pi_{m|I_k} \parallel \pi_m)$, from conducting $k = 1, \dots, 5$ experiments. The green stars are obtained by conducting the experiments with boundary conditions chosen using the SOED procedure with the A- and D-optimality criterion. Note that the A-optimal design should maximize $-\text{trace}(\mathbf{C}_{m|I_k})$, hence minimize $\text{trace}(\mathbf{C}_{m|I_k})$. We plot the latter, since the A-optimal design is often interpreted as the one minimizing the average posterior pointwise variance. The box plot is obtained by using 100 randomly chosen boundary conditions for all five experiments. In all cases, data was synthesized using the true diffusivity field visualized in Figure 6.5.

ACKNOWLEDGEMENTS

This work has been partially funded by the Carl Zeiss-Stiftung through the project “Model-Based AI: Physical Models and Deep Learning for Imaging and Cancer Treatment”. The authors would like to thank Tiangang Cui and Sergey Dolgov for many helpful discussions and access to the developmental version of the DIRT MATLAB package. The authors thank the reviewer for helpful comments and suggestions.

REFERENCES

- [1] A. Alexanderian. “Optimal experimental design for infinite-dimensional Bayesian inverse problems governed by PDEs: a review”. *Inverse Problems* 37.4 (2021), p. 043001. DOI: [10.1088/1361-6420/abe10c](https://doi.org/10.1088/1361-6420/abe10c). arXiv: [2005.12998](https://arxiv.org/abs/2005.12998).
- [2] A. Alexanderian; P. J. Gloor; O. Ghattas. “On Bayesian A- and D-optimal experimental designs in infinite dimensions”. *Bayesian Analysis* 11.3 (2016). DOI: [10.1214/15-ba969](https://doi.org/10.1214/15-ba969).
- [3] A. Alexanderian; R. Nicholson; N. Petra. *Optimal design of large-scale nonlinear Bayesian inverse problems under model uncertainty*. 2022. arXiv: [2211.03952](https://arxiv.org/abs/2211.03952).
- [4] A. Alexanderian; N. Petra; G. Stadler; O. Ghattas. “A-optimal design of experiments for infinite-dimensional Bayesian linear inverse problems with regularized ℓ_0 -sparsification”. *SIAM Journal on Scientific Computing* 36.5 (2014), A2122–A2148. DOI: [10.1137/130933381](https://doi.org/10.1137/130933381).
- [5] A. Alexanderian; N. Petra; G. Stadler; O. Ghattas. “A fast and scalable method for A-optimal design of experiments for infinite-dimensional Bayesian nonlinear inverse problems”. *SIAM Journal on Scientific Computing* 38.1 (2016), A243–A272. DOI: [10.1137/140992564](https://doi.org/10.1137/140992564).

- [6] A. Alexanderian; N. Petra; G. Stadler; I. Sunseri. “Optimal design of large-scale Bayesian linear inverse problems under reducible model uncertainty: good to know what you don’t know”. *SIAM/ASA Journal on Uncertainty Quantification* 9.1 (2021), pp. 163–184. DOI: [10.1137/20m1347292](https://doi.org/10.1137/20m1347292). arXiv: [2006.11939](https://arxiv.org/abs/2006.11939).
- [7] A. Alexanderian; A. K. Saibaba. “Efficient D-optimal design of experiments for infinite-dimensional Bayesian linear inverse problems”. *SIAM Journal on Scientific Computing* 40.5 (2018), A2956–A2985. DOI: [10.1137/17m115712x](https://doi.org/10.1137/17m115712x).
- [8] A. C. Atkinson; A. N. Donev; R. D. Tobias. *Optimum Experimental Designs, with SAS*. Vol. 34. Oxford Statistical Science Series. Oxford: Oxford University Press, 2007.
- [9] A. Attia; A. Alexanderian; A. K. Saibaba. “Goal-oriented optimal design of experiments for large-scale Bayesian linear inverse problems”. *Inverse Problems* 34.9 (2018), p. 095009. DOI: [10.1088/1361-6420/aad210](https://doi.org/10.1088/1361-6420/aad210).
- [10] A. Attia; E. Constantinescu. “Optimal experimental design for inverse problems in the presence of observation correlations”. *SIAM Journal on Scientific Computing* 44.4 (2022), A2808–A2842. DOI: [10.1137/21m1418666](https://doi.org/10.1137/21m1418666).
- [11] A. Attia; S. Leyffer; T. S. Munson. “Stochastic learning approach for binary optimization: application to Bayesian optimal design of experiments”. *SIAM Journal on Scientific Computing* 44.2 (2022), B395–B427. DOI: [10.1137/21m1404363](https://doi.org/10.1137/21m1404363).
- [12] R. Baptista; L. Cao; J. Chen; O. Ghattas; F. Li; Y. M. Marzouk; J. T. Oden. *Bayesian model calibration for block copolymer self-assembly: likelihood-free inference and expected information gain computation via measure transport*. 2022. arXiv: [2206.11343](https://arxiv.org/abs/2206.11343).
- [13] R. Baptista; B. Hosseini; N. B. Kovachki; Y. Marzouk. *Conditional sampling with monotone GANs: from generative models to likelihood-free inference*. 2020. arXiv: [2006.06755](https://arxiv.org/abs/2006.06755).
- [14] R. Baptista; Y. Marzouk; O. Zahm. *On the representation and learning of monotone triangular transport maps*. 2020. arXiv: [2009.10303](https://arxiv.org/abs/2009.10303).
- [15] D. Bigoni; A. P. Engsig-Karup; Y. M. Marzouk. “Spectral tensor-train decomposition”. *SIAM Journal on Scientific Computing* 38.4 (2016), A2405–A2439. DOI: [10.1137/15m1036919](https://doi.org/10.1137/15m1036919).
- [16] M. Brennan; D. Bigoni; O. Zahm; A. Spantini; Y. Marzouk. “Greedy inference with structure-exploiting lazy maps”. *Advances in Neural Information Processing Systems*. Ed. by H. Larochelle; M. Ranzato; R. Hadsell; M. Balcan; H. Lin. Vol. 33. NeurIPS’20. Curran Associates, Inc., 2020, pp. 8330–8342. arXiv: [1906.00031](https://arxiv.org/abs/1906.00031). URL: https://proceedings.neurips.cc/paper_files/paper/2020/file/5ef20b89bab8fed38253e98a12f26316-Paper.pdf.
- [17] S. Chaturantabut; D. C. Sorensen. “Nonlinear model reduction via discrete empirical interpolation”. *SIAM Journal on Scientific Computing* 32.5 (2010), pp. 2737–2764. DOI: [10.1137/090766498](https://doi.org/10.1137/090766498).
- [18] T. Cui. *Fast Forward and Inverse problems solver (FastFInS)*. 2022. URL: <https://github.com/fastfins/fastfins.m>.
- [19] T. Cui. *Deep Inverse Rosenblatt Transport (DIRT)*. 2023. URL: <https://github.com/DeepTransport/deep-tensor>.
- [20] T. Cui; S. Dolgov. “Deep composition of tensor-trains using squared inverse Rosenblatt transports”. *Foundations of Computational Mathematics* 22.6 (2021), pp. 1863–1922. DOI: [10.1007/s10208-021-09537-5](https://doi.org/10.1007/s10208-021-09537-5).
- [21] T. Cui; S. Dolgov; O. Zahm. “Scalable conditional deep inverse Rosenblatt transports using tensor trains and gradient-based dimension reduction”. *Journal of Computational Physics* 485 (2023), p. 112103. DOI: [10.1016/j.jcp.2023.112103](https://doi.org/10.1016/j.jcp.2023.112103). arXiv: [2106.04170](https://arxiv.org/abs/2106.04170).
- [22] T. Cui; K. J. Law; Y. M. Marzouk. “Dimension-independent likelihood-informed MCMC”. *Journal of Computational Physics* 304 (2016), pp. 109–137. DOI: [10.1016/j.jcp.2015.10.008](https://doi.org/10.1016/j.jcp.2015.10.008).
- [23] G. Detommaso; T. Cui; Y. Marzouk; A. Spantini; R. Scheichl. “A Stein variational Newton method”. *Advances in Neural Information Processing Systems*. Ed. by S. Bengio; H. Wallach; H. Larochelle; K. Grauman; N. Cesa-Bianchi; R. Garnett. Vol. 31. Curran Associates, Inc., 2018. URL: https://proceedings.neurips.cc/paper_files/paper/2018/file/fdaa09fc5ed18d3226b3a1a00f1bc48c-Paper.pdf.

- [24] T. J. Dodwell; C. Ketelsen; R. Scheichl; A. L. Teckentrup. “A hierarchical multilevel Markov Chain Monte Carlo algorithm with applications to uncertainty quantification in subsurface flow”. *SIAM/ASA Journal on Uncertainty Quantification* 3.1 (2015), pp. 1075–1108. DOI: [10.1137/130915005](https://doi.org/10.1137/130915005). arXiv: [1303.7343](https://arxiv.org/abs/1303.7343).
- [25] S. Dolgov; K. Anaya-Izquierdo; C. Fox; R. Scheichl. “Approximation and sampling of multivariate probability distributions in the tensor train decomposition”. *Statistics and Computing* 30.3 (2019), pp. 603–625. DOI: [10.1007/s11222-019-09910-z](https://doi.org/10.1007/s11222-019-09910-z). arXiv: [1810.01212](https://arxiv.org/abs/1810.01212).
- [26] S. V. Dolgov; D. V. Savostyanov. “Alternating minimal energy methods for linear systems in higher dimensions”. *SIAM Journal on Scientific Computing* 36.5 (2014), A2248–A2271. DOI: [10.1137/140953289](https://doi.org/10.1137/140953289).
- [27] A. Foster; D. R. Ivanova; I. Malik; T. Rainforth. “Deep adaptive design: amortizing sequential Bayesian experimental design”. *Proceedings of the 38th International Conference on Machine Learning*. Ed. by M. Meila; T. Zhang. Vol. 139. Proceedings of Machine Learning Research. PMLR, 2021, pp. 3384–3395. URL: <https://proceedings.mlr.press/v139/foster21a.html>.
- [28] A. Foster; M. Jankowiak; M. O’Meara; Y. W. Teh; T. Rainforth. “A unified stochastic gradient approach to designing Bayesian-optimal experiments”. *Proceedings of the 23rd International Conference on Artificial Intelligence and Statistics*. Ed. by S. Chiappa; R. Calandra. Vol. 108. Proceedings of Machine Learning Research. PMLR, 2020, pp. 2959–2969. URL: <https://proceedings.mlr.press/v108/foster20a.html>.
- [29] A. Gelman; X.-L. Meng. “Simulating normalizing constants: from importance sampling to bridge sampling to path sampling”. *Statistical Science* 13.2 (1998). DOI: [10.1214/ss/1028905934](https://doi.org/10.1214/ss/1028905934).
- [30] A. L. Gibbs; F. E. Su. “On choosing and bounding probability metrics”. *International Statistical Review* 70.3 (2002), pp. 419–435. DOI: [10.2307/1403865](https://doi.org/10.2307/1403865).
- [31] A. Gorodetsky; S. Karaman; Y. Marzouk. “A continuous analogue of the tensor-train decomposition”. *Computer Methods in Applied Mechanics and Engineering* 347 (2019), pp. 59–84. DOI: [10.1016/j.cma.2018.12.015](https://doi.org/10.1016/j.cma.2018.12.015).
- [32] M. Griebel; H. Harbrecht. “Analysis of tensor approximation schemes for continuous functions”. *Foundations of Computational Mathematics* 23.1 (2021), pp. 219–240. DOI: [10.1007/s10208-021-09544-6](https://doi.org/10.1007/s10208-021-09544-6).
- [33] E. Haber; L. Horesh; L. Tenorio. “Numerical methods for experimental design of large-scale linear ill-posed inverse problems”. *Inverse Problems* 24.5 (2008), pp. 055012, 17. DOI: [10.1088/0266-5611/24/5/055012](https://doi.org/10.1088/0266-5611/24/5/055012).
- [34] W. K. Hastings. “Monte Carlo sampling methods using Markov chains and their applications”. *Biometrika* 57.1 (1970), pp. 97–109. DOI: [10.1093/biomet/57.1.97](https://doi.org/10.1093/biomet/57.1.97).
- [35] X. Huan. “Numerical Approaches for Sequential Bayesian Optimal Experimental Design”. PhD thesis. 2015. URL: <http://hdl.handle.net/1721.1/101442>.
- [36] X. Huan; Y. Marzouk. “Gradient-based stochastic optimization methods in Bayesian experimental design”. *International Journal for Uncertainty Quantification* 4.6 (2014), pp. 479–510. DOI: [10.1615/int.j.uncertaintyquantification.2014006730](https://doi.org/10.1615/int.j.uncertaintyquantification.2014006730).
- [37] X. Huan; Y. M. Marzouk. “Simulation-based optimal Bayesian experimental design for nonlinear systems”. *Journal of Computational Physics* 232.1 (2013), pp. 288–317. DOI: [10.1016/j.jcp.2012.08.013](https://doi.org/10.1016/j.jcp.2012.08.013).
- [38] K. Koval; A. Alexanderian; G. Stadler. “Optimal experimental design under irreducible uncertainty for linear inverse problems governed by PDEs”. *Inverse Problems* 36.7 (2020), p. 075007. DOI: [10.1088/1361-6420/ab89c5](https://doi.org/10.1088/1361-6420/ab89c5).
- [39] J. Kruse; G. Detommaso; U. Köthe; R. Scheichl. *HINT: hierarchical invertible neural transport for density estimation and Bayesian inference*. 2019. arXiv: [1905.10687](https://arxiv.org/abs/1905.10687).
- [40] D. V. Lindley. “On a measure of the information provided by an experiment”. *The Annals of Mathematical Statistics* 27.4 (1956), pp. 986–1005. DOI: [10.1214/aoms/1177728069](https://doi.org/10.1214/aoms/1177728069).
- [41] Q. Liu; D. Wang. “Stein variational gradient descent: a general purpose Bayesian inference algorithm”. *Advances in Neural Information Processing Systems*. Ed. by D. Lee; M. Sugiyama; U. Luxburg; I. Guyon; R. Garnett. Vol. 29. NIPS’16. Curran Associates, Inc., 2016. URL: <https://paperswithcode.com/sota/bayesian-inference-on-nips16/liu2016stein>.

- [roceedings.neurips.cc/paper_files/paper/2016/file/b3ba8f1bee1238a2f37603d90b58898d-Paper.pdf](https://proceedings.neurips.cc/paper_files/paper/2016/file/b3ba8f1bee1238a2f37603d90b58898d-Paper.pdf).
- [42] Q. Long; M. Scavino; R. Tempone; S. Wang. “Fast estimation of expected information gains for Bayesian experimental designs based on Laplace approximations”. *Computer Methods in Applied Mechanics and Engineering* 259 (2013), pp. 24–39. DOI: [10.1016/j.cma.2013.02.017](https://doi.org/10.1016/j.cma.2013.02.017).
 - [43] Y. Marzouk; T. Moselhy; M. Parno; A. Spantini. “Sampling via measure transport: an introduction”. *Handbook of Uncertainty Quantification*. Springer International Publishing, 2016, pp. 1–41. DOI: [10.1007/978-3-319-11259-6_23-1](https://doi.org/10.1007/978-3-319-11259-6_23-1). arXiv: [1602.05023](https://arxiv.org/abs/1602.05023).
 - [44] T. A. E. Moselhy; Y. M. Marzouk. “Bayesian inference with optimal maps”. *Journal of Computational Physics* 231.23 (2012), pp. 7815–7850. DOI: [10.1016/j.jcp.2012.07.022](https://doi.org/10.1016/j.jcp.2012.07.022).
 - [45] I. Neitzel; K. Pieper; B. Vexler; D. Walter. “A sparse control approach to optimal sensor placement in PDE-constrained parameter estimation problems”. *Numerische Mathematik* 143.4 (2019), pp. 943–984. DOI: [10.1007/s00211-019-01073-3](https://doi.org/10.1007/s00211-019-01073-3).
 - [46] I. Oseledets; E. Tyrtyshnikov. “TT-cross approximation for multidimensional arrays”. *Linear Algebra and its Applications* 432.1 (2010), pp. 70–88. DOI: [10.1016/j.laa.2009.07.024](https://doi.org/10.1016/j.laa.2009.07.024).
 - [47] G. Papamakarios; E. Nalisnick; D. Jimenez Rezende; S. Mohamed; B. Lakshminarayanan. “Normalizing flows for probabilistic modeling and inference”. *Journal of Machine Learning Research* 22.57 (2021), pp. 1–64. URL: <https://www.jmlr.org/papers/v22/19-1028.html>.
 - [48] M. D. Parno; Y. M. Marzouk. “Transport map accelerated Markov Chain Monte Carlo”. *SIAM/ASA Journal on Uncertainty Quantification* 6.2 (2018), pp. 645–682. DOI: [10.1137/17m1134640](https://doi.org/10.1137/17m1134640).
 - [49] A. Pázman. *Foundations of Optimum Experimental Design*. Vol. 14. Mathematics and its Applications. Translated from the Czech. Springer, 1986.
 - [50] F. Pukelsheim. *Optimal Design of Experiments*. Vol. 50. Classics in Applied Mathematics. Reprint of the 1993 original. Philadelphia, PA: Society for Industrial and Applied Mathematics (SIAM), 2006. DOI: [10.1137/1.9780898719109](https://doi.org/10.1137/1.9780898719109).
 - [51] P. B. Rohrbach; S. Dolgov; L. Grasedyck; R. Scheichl. “Rank bounds for approximating Gaussian densities in the tensor-train format”. *SIAM/ASA Journal on Uncertainty Quantification* 10.3 (2022), pp. 1191–1224. DOI: [10.1137/20m1314653](https://doi.org/10.1137/20m1314653).
 - [52] M. Rosenblatt. “Remarks on a multivariate transformation”. *The Annals of Mathematical Statistics* 23.3 (1952), pp. 470–472. DOI: [10.1214/aoms/1177729394](https://doi.org/10.1214/aoms/1177729394).
 - [53] D. Uciński. *Optimal Measurement Methods for Distributed Parameter System Identification*. Systems and Control Series. Boca Raton, FL: CRC Press, 2005. DOI: [10.1201/9780203026786](https://doi.org/10.1201/9780203026786).
 - [54] C. Villani. *Optimal Transport*. Vol. 338. Grundlehren der Mathematischen Wissenschaften. Springer Berlin Heidelberg, 2009. DOI: [10.1007/978-3-540-71050-9](https://doi.org/10.1007/978-3-540-71050-9).
 - [55] K. Wu; T. O’Leary-Roseberry; P. Chen; O. Ghattas. *Large-scale Bayesian optimal experimental design with derivative-informed projected neural network*. 2022. arXiv: [2201.07925](https://arxiv.org/abs/2201.07925).
 - [56] Y. Zhao; T. Cui. *Tensor-train methods for sequential state and parameter learning in state-space models*. 2023. arXiv: [2301.09891](https://arxiv.org/abs/2301.09891).

(K. Koval) INTERDISCIPLINARY CENTER FOR SCIENTIFIC COMPUTING, HEIDELBERG UNIVERSITY, 69120 HEIDELBERG, GERMANY

Email address: karina.koval@iwr.uni-heidelberg.de

URL: <https://scoop.iwr.uni-heidelberg.de>

(R. Herzog) INTERDISCIPLINARY CENTER FOR SCIENTIFIC COMPUTING AND INSTITUTE FOR MATHEMATICS, HEIDELBERG UNIVERSITY, 69120 HEIDELBERG, GERMANY

Email address: roland.herzog@iwr.uni-heidelberg.de

URL: <https://scoop.iwr.uni-heidelberg.de>

(R. Scheichl) INSTITUTE FOR MATHEMATICS AND INTERDISCIPLINARY CENTER FOR SCIENTIFIC COMPUTING, HEIDELBERG UNIVERSITY, 69120 HEIDELBERG, GERMANY

Email address: robert.scheichl@uni-heidelberg.de

URL: <https://katana.iwr.uni-heidelberg.de/people/rob/>